Geochemistry, Geophysics, Geosystems®

RESEARCH ARTICLE
10.1029/2024GC011620

Paleomagnetic Secular Variations in North Greenland Around 81°N Over the Last 6,000 Years

Juliette Girard[1], Brendan T. Reilly[2], Guillaume St-Onge[1], France Lagroix[3], Jean-Carlos Montero-Serrano[1], Joesph S. Stoner[4], and Anne E. Jennings[5]

[1]Institut des sciences de la mer (ISMER), Canada Research Chair in Marine Geology, Université du Québec à Rimouski (UQAR), GEOTOP, Rimouski, QC, Canada, [2]Lamont-Doherty Earth Observatory, Columbia University, Palisades, NY, USA, [3]Institut de Physique du Globe de Paris, Université Paris Cité, CNRS, Paris, France, [4]College of Earth, Ocean, and Atmospheric Sciences, Oregon State University, Corvallis, OR, USA, [5]Institute of Arctic and Alpine Research, University of Colorado, Boulder, CO, USA

Abstract We investigate full vector paleomagnetic changes recorded in high-resolution sediments of Petermann Fjord, North Greenland, deposited over the last 6 kyr, in the context of the recent rapid changes in the geomagnetic field. A Paleomagnetic Secular Variation (PSV) stack (inclination, declination, and relative paleointensity) was reconstructed using four marine sediment cores with an independent age model constrained by seven radiocarbon ages. Magnetic investigations demonstrate that the paleomagnetic signal is carried by low coercivity ferrimagnetic minerals and is well reproduced in all cores, attesting to the quality and reliability of the paleomagnetic recording of these sediments. This signal is broadly consistent in directional changes with distant records in North America and the northern North Atlantic at centennial and millennial timescales, and has millennial scale intensity variations that are consistent with model predictions. The offset between a magnetization age determined through comparison with a northern North Atlantic PSV reference curve, GREENICE, and the radiocarbon age model indicates either a reasonable lock-in depth of magnetization (~11 cm from the coretop) or centennial-scale reservoir age variation through time in the fjord. Reconstructed virtual geomagnetic pole (VGP) migration for the last 6 kyr shows that the recent migration of the magnetic North Pole is consistent with secular paleomagnetic variations on geologic timescales. Our results suggest that magnetic field intensity variations (temporal and spatial) are linked to magnetic flux lobe dynamics and influence the VGP migration.

Plain Language Summary The magnetic field of the Earth is generated by convection in the outer core of the Earth. Magnetic sediments deposited on the ocean seafloor record the Earth's magnetic field and are important archives of its past fluctuations (intensity and direction). Studying the geomagnetic field is important as it gives us information about processes in the Earth's core and can be used for correlating sediment cores together and for establishing the chronology of sedimentary sequences. In this study, we used sediment cores from Petermann Fjord (Nares Strait, Northern Greenland) to study past geomagnetic variations. Petermann Fjord is an excellent site to conduct such studies because of its close location to the North Magnetic Pole (NMP) and because of the high sediment accumulation rates that enable us to conduct studies with a high temporal resolution. We hypothesize that the NMP migration during the last millennia could have been driven by strong regional intensity features of the geomagnetic field and that the recent rapid migration of the NMP is not unusual because such amplitudes of migration happened in the past, without necessary leading to a reversal of the poles.

Key Points:

- Paleomagnetic secular variations (inclination, declination and relative paleointensity) reconstituted in Petermann Fjord for the last 6 kyr
- Geomagnetic flux lobes could play a role in the virtual geomagnetic pole migration
- The recent migration of the North Magnetic Pole is consistent with Holocene paleomagnetic secular variations

Supporting Information:

Supporting Information may be found in the online version of this article.

Correspondence to:

J. Girard,
juliette.girard@uqar.ca

Citation:

Girard, J., Reilly, B. T., St-Onge, G., Lagroix, F., Montero-Serrano, J.-C., Stoner, J. S., & Jennings, A. E. (2024). Paleomagnetic secular variations in North Greenland around 81°N over the last 6,000 years. *Geochemistry, Geophysics, Geosystems*, *25*, e2024GC011620. https://doi.org/10.1029/2024GC011620

Received 19 APR 2024
Accepted 5 SEP 2024

1. Introduction

The North Magnetic Pole (NMP) was directly located for the first time in 1831 in the Canadian Arctic (Ross, 1834). Direct observations from 1831 to 2007 and recent satellite observations show a clear migration of the NMP over more than 1,700 km since the early twentieth century from the Canadian Arctic into the Arctic Ocean and toward Siberia (Livermore et al., 2020; Olsen & Mandea, 2007). Recent data from the Resolute Bay observatory show an increase in the NMP migration velocity from 9 to 41 km/year during the 1970s and up to 60 km/year in 2003 (NOAA, 2021). According to the current World Magnetic Model (National Centers for Environmental Information, 2023), the 2023 North Magnetic Dip Pole is located at 146.826°E 86.146°N (National Centers for Environmental Information, 2022). NMP migration is coupled with a decrease in the geomagnetic dipole moment by 10% since the first mathematical reconstruction by Gauss (1833)

(Gubbins, 2008). The modern northern Hemisphere intensity pattern is not that of a perfect dipole; rather, sub-arctic regions of high field intensity, called geomagnetic flux lobes, can be observed in North America, Siberia and Europe (Bloxham & Jackson, 1992; Bloxham et al., 1989; Jackson et al., 2000). The NMP migration is currently following a straight path between two of these geomagnetic flux lobes (Livermore et al., 2020). Here, we ask if this recent rapid migration of the NMP is unusual relative to pre-1831 variations and use the high-resolution (>50 cm/ka) sedimentary record of Petermann Fjord, North Greenland (~81°N), as a high Arctic geologic observatory, to answer this question.

The geomagnetic field displays unique variations in the High Arctic region (Bloxham et al., 1989; Chulliat, Hulot, & Newitt, 2010; Chulliat, Hulot, Newitt, Orgeval, 2010; Haines & Newitt, 1997; Jackson et al., 2000; Newitt et al., 2002; Olson & Aurnou, 1999; St-Onge & Stoner, 2011) and pioneer studies of the Baffin Bay sediments using PSV revealed excursions at high latitudes (Simon et al., 2012, 2016; Thouveny, 1988), which makes the Arctic a pertinent zone to study paleomagnetism. Because of the Coriolis effect and the solid inner Earth core, different flow regimes operate in the outer core, separated by a cylinder, tangent to the inner core and parallel to the rotation axis (e.g., Aurnou et al., 2003; Hollerbach & Jones, 1993; Lawrence et al., 2009). The projection of the tangent cylinder (TC) at the Earth's surface is observed in the Arctic (70°N), and presents low geomagnetic intensities (Hulot et al., 2002; Olson & Aurnou, 1999). The higher geomagnetic intensity at flux lobes arises from the convection outside the TC (Bloxham & Gubbins, 1985). Previous paleomagnetic studies in the European Arctic (Caricchi et al., 2020) and northern North Atlantic (Stoner et al., 2013) demonstrated that flux lobes and intensity variations likely play a role in the variation of the NMP migration on geologic timescales. However, expanding these observations through paleomagnetic reconstructions in the Arctic is often challenging due to complexities in chronologies that stem from lack of datable material, large uncertainties in old carbon effects, and low or variable sedimentation rates.

The sediments of Petermann Fjord have shown great potential as a high Arctic Holocene paleomagnetic site, with previous studies dedicated to establishing a chronostratigraphy to study deglaciation and floating ice tongue history (Jennings et al., 2022; Reilly et al., 2019). Here we revisit the Petermann Fjord paleomagnetic record with a new core, additional radiocarbon data, new rock magnetic data, and estimates of relative paleointensity (RPI) to establish a new full vector PSV reconstruction with an independent age model that can be evaluated against other Northern Hemisphere records and global models. The high sediment accumulation rates or SAR (~60 cm/ka) and proximity to the NMP make this site ideal for assessing the role of the TC and geomagnetic flux lobes on the paleomagnetic variations and NMP migration (St-Onge & Stoner, 2011).

2. Materials and Methods

2.1. Petermann Fjord Sediment Cores

Petermann Fjord is a 1,100 m deep, 90 km long and 20 km wide fjord located in Nares Strait (Jakobsson et al., 2018), which is connected with the Lincoln Sea to the North and Baffin Bay to the southwest (Figure 1a). Sediments are primarily derived from Lower Paleozoic sedimentary carbonate rocks and inland, sub-ice crystalline rocks (Dawes et al., 2000), delivered primarily by suspension settling from glacier meltwater plumes and ice-rafted debris, with an increased influence of downslope transport in the fjord's deep basin (Hogan et al., 2020; Reilly et al., 2019). SAR on bathymetric highs away from downslope deposits range from 50 to 90 cm/ka and average ~60 cm/ka in the cores studied here (Reilly et al., 2019). While this study focuses on the paleomagnetic signals in these sediments, recent changes to the floating Petermann Ice Tongue have motivated a number of studies focused on the oceanography, climate, and ice sheet histories of the region (e.g., Detlef et al., 2021; Heuzé et al., 2017; Hogan et al., 2020; Jakobsson et al., 2018; Jennings et al., 2022; Reilly et al., 2019; Washam et al., 2019).

Core AMD1902-10GC (hereafter referred to as 10GC, Figure 1b and Table 1) was recovered in Petermann Fjord during the ArcticNet expedition in 2019 onboard the Canadian Coast Guard Ship Amundsen using a 3 m gravity corer. On board, the cores were cut into 1.5 m sections, and new data were generated for this study, as described below. The top of core 10GC was most likely lost during coring. However, not knowing how much was lost, we still define the top of the core at 0 cm in the following figures and text. OD1507-04GC, -41GC and -40TC (Figure 1b and Table 1) were collected in Petermann Fjord during the Petermann 2015 Expedition onboard the Swedish Icebreaker Oden (OD1507), with data and methods previously reported by Reilly et al. (2019).

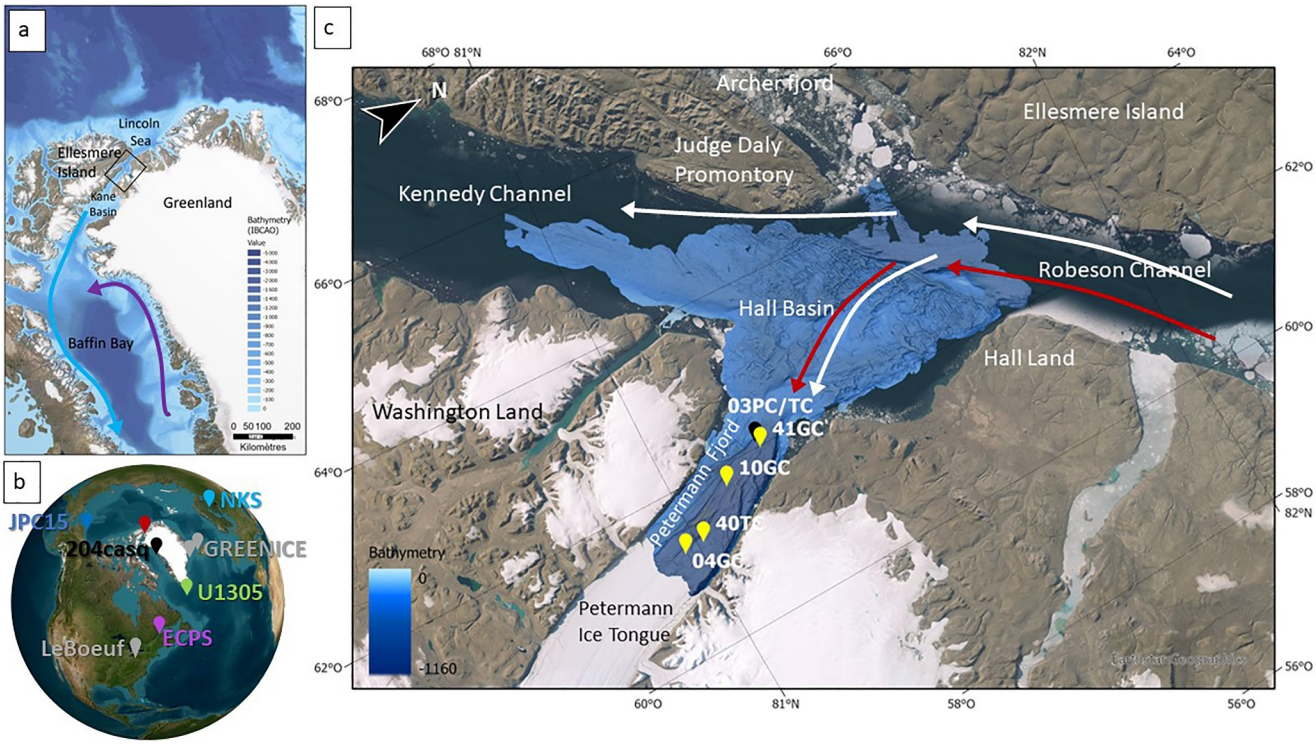

Figure 1. (a) Location of study site in Nares Strait, with bathymetric data from the International Bathymetric Chart of the Arctic Ocean (IBCAO, Jakobsson et al., 2020). Blue arrows represent the cold polar waters becoming the Baffin Current, Purple arrows represent the West Greenland Current. (b) Location of the comparison records mentioned in this study. (c) Map of the study sites in Petermann Fjord. Multibeam bathymetry of the Petermann Fjord and Hall Basin were obtained from Jakobsson et al. (2018). Black dots = cores composing the outer fjord splice; yellow dots = cores composing the stack. 10GC was collected during AMD1902 expedition (REF), 03PC/TC, 41GC, 04GC, 40TC during OD1507 (Reilly et al., 2019). Surface Polar Waters are represented by white arrows and subsurface Atlantic Waters are represented by red arrows.

2.2. Physical Properties: X-Ray Imaging and Multi-Sensor Core Logger Analysis

The whole sections of core 10GC were scanned with a GEOTEK X-ray Computed Tomography (X-CT) system at ISMER (Québec, Canada) to obtain digital X-ray images in greyscale to detect density changes and identify different sedimentary structures (St-Onge et al., 2007). Physical and magnetic properties of core 10GC were measured at 1 cm intervals using a GEOTEK Multi Sensor Core Logger at ISMER (St-Onge et al., 2007), including P-wave velocity and wet bulk density on whole cores. Low field volumetric magnetic susceptibility (k_{LF}) was measured both on the whole core and half sections with a Bartington Instruments M2SEI point sensor at 1 cm intervals. Chemical composition was measured on the half-sections of core 10GC with an energy-dispersive Olympus Innov-X DELTA portable X-ray fluorescence (pXRF) analyzer at 1 cm intervals. Half-sections were digitally photographed with a GEOTEK Geoscan IV imaging system. Diffuse spectral reflectance measurements were conducted at 1 cm intervals using a Minolta CM-2600d spectrophotometer at ISMER. The data acquired were expressed according to the color space of the International Commission on Illumination: L* black (0) to white (100), a* green (−60) to red (+60), and b* blue (−60) to yellow (+60) (Debret et al., 2011; St-Onge et al., 2007).

Table 1
Sediment Cores Used in This Study

Core	Location	Latitude (°)	Longitude (°)	Depth (mbsl)	Length (m)	References
AMD1902-10GC	Petermann Fjord (~70 km from grounding line)	81.102	−61.746	1,085	2.723	Montero-Serrano and Brossard (2019)
OD1507-04GC	Petermann Fjord (52 km from grounding line)	80.970	−61.253	968	4.46	Reilly et al. (2019)
OD1507-41GC	Petermann Fjord (80 km from grounding line)	81.194	−61.977	991	4.4	
OD1507-40TC	Petermann Fjord (56 km from grounding line)	81.010	−61.271	932	3.188	

The physical and chemical properties of cores 40TC, 41GC and 04GC were obtained by Reilly et al. (2019). While many data sets are comparable, XRF measurements were performed with an ITRAX XRF core scanner with a Mo tube and 5 s exposure time at the Oregon State University Marine and Geology Repository (USA). Accordingly, absolute values differ between the two XRF systems, and only relative comparisons are possible. In this study, we only used Ti/Ca as a proxy for the terrigenous sediment composition (Croudace & Rothwell, 2015) to correlate all sediment cores. In this system, it reflects the relative detrital input from carbonate rock erosion (detrital calcite, low Ti/Ca) versus from crystalline basement rock erosion (higher Ti/Ca) (Jennings et al., 2022; Reilly et al., 2019).

2.3. Grain Size Analysis

Grain size measurements (<2 mm fraction) on core 10GC were conducted with a Malvern-Panalytical Mastersizer 3000 laser particle size analyzer at ISMER on non-pretreated sediment samples at 10 cm intervals. Prior to the analyses, 0.5 g of sediment was deflocculated with a solution composed of 30 mL of sodium hexametaphosphate (concentration 20 g/L) and 70 mL of water and by agitating the mixture for at least 3 hr before analysis using an in-house rotator. After measurement, grain-size distribution and statistical parameters were calculated with the GRADISTAT Excel spreadsheet version 9.1 (Blott & Pye, 2001) to obtain different parameters such as the D90 (μm). Ice rafted debris (IRD) abundance was determined by counting the >2 mm fraction on the X-CT images in contiguous 2-cm windows (Grobe, 1987). All of these grain size parameters can help to document lithological changes in the core sediment.

2.4. Continuous Paleomagnetic Measurements

U-channels were sampled in core 10GC using square plastic tubes of 4 cm^2 and up to 1.5 m long (e.g., Weeks et al., 1993) and were then used to conduct continuous magnetic measurements at 1 cm intervals with a 2G Enterprises 755SRM-1.65 cryogenic magnetometer at ISMER. It enabled us to first measure the Natural Remanent Magnetization (NRM) and then conduct stepwise demagnetization from 0 to 80 mT at 5 mT increments and at 10 mT increments from 80 to 100 mT using an alternating field (AF). Anhysteretic remanent magnetization (ARM) was induced with a 100 mT peak AF field and a 50 μT direct current biasing field. U-channels were then stepwise demagnetized in the same way as the NRM. A pulse magnetizer was used to induce an isothermal remanent magnetization at 300 mT (IRM) and 950 mT (representing a saturation isothermal remanent magnetization [SIRM]), which were then subsequently demagnetized and measured at 5 mT increments from 0 to 80 mT for the IRM and at 0, 10, 30, and 50 mT for the SIRM.

After each measurement, data were checked, and flux jumps corrected if necessary with the UPmag MATLAB software (Xuan & Channell, 2009). The characteristic remanent magnetization was then calculated by principal component analysis (PCA; Kirschvink, 1980) with the Mazaud Excel spreadsheet (Mazaud, 2005) using the 20–60 mT steps, providing declination and inclination data as well as maximum angular deviation (MAD) and median destructive field (MDF) values. Due to the response function of the magnetometer, values are smoothed over a 7–8 cm interval (Philippe et al., 2018; Weeks et al., 1993). To avoid edge effects, we do not consider the 4 cm interval at the top and bottom of each u-channel.

The MDF is the field intensity required to remove half of the initial remanence and is a measure of the unblocking field spectrum of the remanence-carrying grains assemblage of the NRM, ARM, or IRM. The k_{ARM}/k_{LF} ratio is a parameter sensitive to changes in magnetic grain size if the magnetic mineralogy is dominated by magnetite and varies inversely with magnetic grainsize (Banerjee et al., 1981; King et al., 1982).

MAD values are one of several indicators of the quality of the directional data (Kirschvink, 1980). High MAD values generally result from complex magnetization with different coercivities and/or sedimentary processes such as turbidity currents and debris flows (Lévesque et al., 2020) and therefore must be carefully used. Zijderveld diagrams (orthogonal projections; Zijderveld, 1967) document the demagnetization behavior (Figure S2 in Supporting Information S1).

Previously reported paleomagnetic measurements from Reilly et al. (2019) were measured on a nearly identical 2G magnetometer at the Oregon State University Paleo- and Environmental Magnetism Laboratory. A previous study has shown that both magnetometers are well intercalibrated (Velle et al., 2021).

Table 2
Radiocarbon Results

Core	Independent depth (cm)	Correlated equivalent depth (cm)	Lab. number	$\delta^{13}C$ (‰)	Dated material	Uncalibrated age (yr)	Error ^{14}C ± (yr)	Median calibrated age (yr BP)	Min-max calibrated ages (yr BP)
03UW	52–54	40.87	ANU#56605	−1.2	Mixed benthic foraminifera	1,421	26	410	188–632
10GC	96–100	79.33	AWI#10207.1.1	−7.2	30% planktic (N. *pachyderma* s.) 70% benthic	1,784	60	913	669–1,213
41GC	*62–64*	*91.72*	*ANU#17240*	*−1.65*	*Mixed benthic*	*2,578*	*33*	*Too old (remobilized material) Not calibrated*	
03UW	229–231	188.72	ANU#56606	−2.2	Mixed benthic	3,427	27	2,718	2,460–3,022
41GC	166–168	195.72	ANU#56603	−1.82	E. *excavatum*	3,567	26	2,847	2,592–3,150
10GC	251–253	232	AWI#10208.1.1	−4.9	30% planktic (N. *pachyderma* s.) 70% benthic	4,277	66	3,593	3,286–3,928
41GC	292–296	322.72	ANU#56604	−1.7	N. *pachyderma* (s)	5,697	30	5,425	5,057–5,771
41GC	374–376	403.72	ANU#53516	−1.4	C. *neoteretis*	7,174	53	7,023	6,635–7,391

Note. The age in italics was not used for the age-depth model. Radiocarbon ages were calibrated using the Marine20 (Heaton et al., 2020) calibration curve with a $\Delta R = 430 \pm 145$ years in the R package "rbacon" (Blaauw & Christen, 2011).

2.5. Rock Magnetic Measurements

A susceptibility meter AGICO KLY-3 was used to measure the temperature-dependent magnetic susceptibility of seven samples of core 10GC (10, 25, 40, 50, 130, 250 cm) in air. The intervals of interest were chosen based on continuous magnetic measurements to determine the magnetic mineralogy and granulometry of the remanence carriers. Samples were heated up to 700°C and then cooled down back to room temperature to notably detect the Curie temperature (Dunlop & Ozdemir, 2007), the temperature at which a mineral loses its permanent magnetization.

Discrete magnetic measurements on core 10GC samples were conducted on a Princeton Measurements vibrating sample magnetometer (VSM) at the Institut de Physique du Globe de Paris (IPGP, France). Hysteresis loops, FORC diagrams (First order reversal curves; Roberts et al., 2019, 2022) and IRM acquisition curves were measured for the same samples before and after heating. Dia/paramagnetic correction (70%) was applied to the hysteresis loops, which are used to identify the magnetic domain state of a mineral (e.g., Day et al., 1977). Additional hysteresis loops were made on OD1507 samples on a VSM at Western Washington University (USA). Magnetic parameters were derived from the hysteresis loops: coercive force (Hc), remanent coercive force (Hcr), saturation magnetization (Ms) and saturation remanence (Mrs). The resulting coercivity and remanence ratios (Hcr/Hc; Mrs/Ms) and the shape of the hysteresis loops are indicative of the magnetic mineralogy and grain size and enable to estimate the magnetic domains (Day et al., 1977; Dunlop, 2002). IRM acquisition curves were measured on the VSM. S-ratios were calculated according to the following equation $\text{S-ratio} = 0.5 \times \left(1 - \frac{\text{IRM}_{-300\text{mT}}}{\text{SIRM}}\right)$ (Bloemendal et al., 1988). To determine the coercivity components of the samples, IRM acquisition curves were "unmixed" (Table S3 in Supporting Information S1) using the online software MAX UnMix (Maxbauer et al., 2016). FORC measurements were processed using the FORCinel software (Harrison & Feinberg, 2008).

2.6. Chronology

Two intervals of 4 cm in core 10GC were sieved at 100 and 150 µm and 2 mm. Foraminifera were picked from the dry fractions 150 µm to 2 mm and 100–150 µm at the University of New Brunswick. The samples were then sent to the Alfred Wegener Institute in Bremerhaven to conduct carbon dating analyses using a Mini Carbon Dating System MICADAS. Five other radiocarbon ages from Reilly et al. (2019) were also used in the age model (Table 2).

The Marine20 ΔR value was calculated using the value $\Delta R = 188 \pm 91$ for the Canadian Artic Archipelago (Pieńkowski et al., 2022) and adding the age offset between Holocene bottom and surface waters in Nares Strait 240 ± 20 (Jennings et al., 2022), leading to a $\Delta R = 430 \pm 95$ years. As the ΔR is uncertain in the Fjord, and to account for possible local variations (in comparison to Nares Strait) in oceanographic circulation, sea ice cover, meltwater, reservoir age variation through time and the difference between planktic and benthic foraminifera, an

uncertainty of ±50 years was added, leading to a final Marine20 value of ΔR = 430 ± 145 years. In Reilly et al. (2019), one of the presented age models, M2, includes a 20 cm lock-in-depth and is calculated with a ΔR = 570 years using the Marine13 calibration curve. For the Holocene, Marine20 ΔR values are about 150 years less than the Marine13 ΔR values. Therefore, the independently derived ΔR value used in the present study is consistent with the M2 ΔR value in Reilly et al. (2019). Based on studies of ocean circulation in the fjord, we consider the age offset between benthic and planktonic foraminifera to be negligible (Heuzé et al., 2017; Jakobsson et al., 2018; Jennings et al., 2020, 2022; Johnson et al., 2011; Münchow et al., 2011, 2016) and near modern mixed planktonic, mixed benthic, and species specific (Cassidulina neoteretis) return similar ages (Reilly et al., 2019). For that reason, a common value of ΔR was used for radiocarbon dates obtained from planktic and benthic foraminifera. The R package "rbacon" version 3.2.0 (Blaauw & Christen, 2011) was used to build the age models using the calibration curve Marine20 (Heaton et al., 2020) and attributing an age of 0 (±65) at 7 cm depth due to vertical compaction of the top of the core 40TC during transport after coring.

3. Results

3.1. Lithology

High-resolution digital images (Figure 2a) and visual description of the split core indicate differences between lithologic units: reddish brown clay (0–7 cm), pinkish gray clay (7–68 cm) with fine sand intervals (20–23 cm and 61–63 cm) and fine laminations (50–54 cm), homogeneous grayish brown clay (68–124 cm) with fine sand-silt intervals (75–76 cm, 108–110 cm, 117–118 cm), IRD-rich brown clay (125–146 cm), brown clay with pinkish gray clay laminations (146–184 cm), and IRD-rich light gray clay (185–269 cm). Rock fragments (cm-scale grains) can be seen on the X-CT images as well as the laminations in the top part of the core (0–50 cm).

Point source k_{LF} (Figure 2a) shows variations around $50 \cdot 10^{-5}$ SI, and a transition around 180 cm depth toward slightly lower values ($\sim 30 \cdot 10^{-5}$ SI). The same transition is observed in the a* profile, with higher amplitude variations in the 0–180 cm interval and a decrease in the average value and the amplitude variations at the bottom of the core (180–257 cm). The Ti/Ca ratio revealed higher amplitude variations in the 0–180 cm interval and lower amplitude variations in the bottom of the core (180–257 cm).

The grain size is homogeneous throughout the entire core: <20% clay, <20% sand and ~60%–70% silt, with 20 μm < D (90) < 30 μm and peaks >40 μm at the top (20 cm) and bottom (250 cm) of the core. There is a low number of >2 mm clasts (0–2 clasts) or IRD in the top 70 cm of the core, with increasing concentrations toward the bottom, up to 6 clasts. Statistics results from GRADISTAT treatment are presented in Supporting Information S1 (Table S1 in Supporting Information S1).

3.2. Continuous Paleomagnetic Measurements

k_{ARM}/k (Figure 2a) presents a similar transition at 180 cm toward higher values as well as a long term trend toward lower values up the core, consistent with a finer magnetic mineralogy in the bottom part of the core (180–250 cm).

In the top 65 cm of the core, MDF_{NRM} values display variations between 35 and 55 mT, possibly indicating the presence of higher coercivity magnetic minerals (Dankers, 1981; Stoner & St-Onge, 2007), whereas the lower values in the rest of the core (~30 mT) are characteristic of ferrimagnetic, low coercivity minerals such as magnetite (Dankers, 1981). MDF_{ARM} and MDF_{IRM}, which are indicators of the coercivity of the magnetic assemblages responding to ARM and IRM, respectively (Stoner & St-Onge, 2007) are both lower than the MDF_{NRM} values and show similar variations in the top part of the core 0–65 cm, which reinforces the hypothesis of higher coercivity grains in that interval, activated by the IRM.

Overall, the physical and magnetic properties of this core indicate a change in the magnetic mineralogy at ~65 cm (MDF) and another change at 190 cm in the lithology (Ti/Ca, a*, k_{LF}, k_{ARM}/k_{LF}). Based on the precedent results, the core can be split into three lithologic units:

- 0–65 cm: pink-gray clay, $k_{LF} \sim 50 \cdot 10^{-5}$ SI, a* ~ 5, high amplitude variations of Ti/Ca, low IRD content, higher MDF between 35 and 65 mT, stable k_{ARM}/k_{LF} (5–13)
- 65–190 cm: brown clay with color variations from pink to gray, IRD enrichment, higher variations of k_{LF} ($40–70 \cdot 10^{-5}$ SI), Ti/Ca, stable MDF close to 30 mT, a* ~ 4.5, stable k_{ARM}/k_{LF} (8–13)

10.1029/2024GC011620

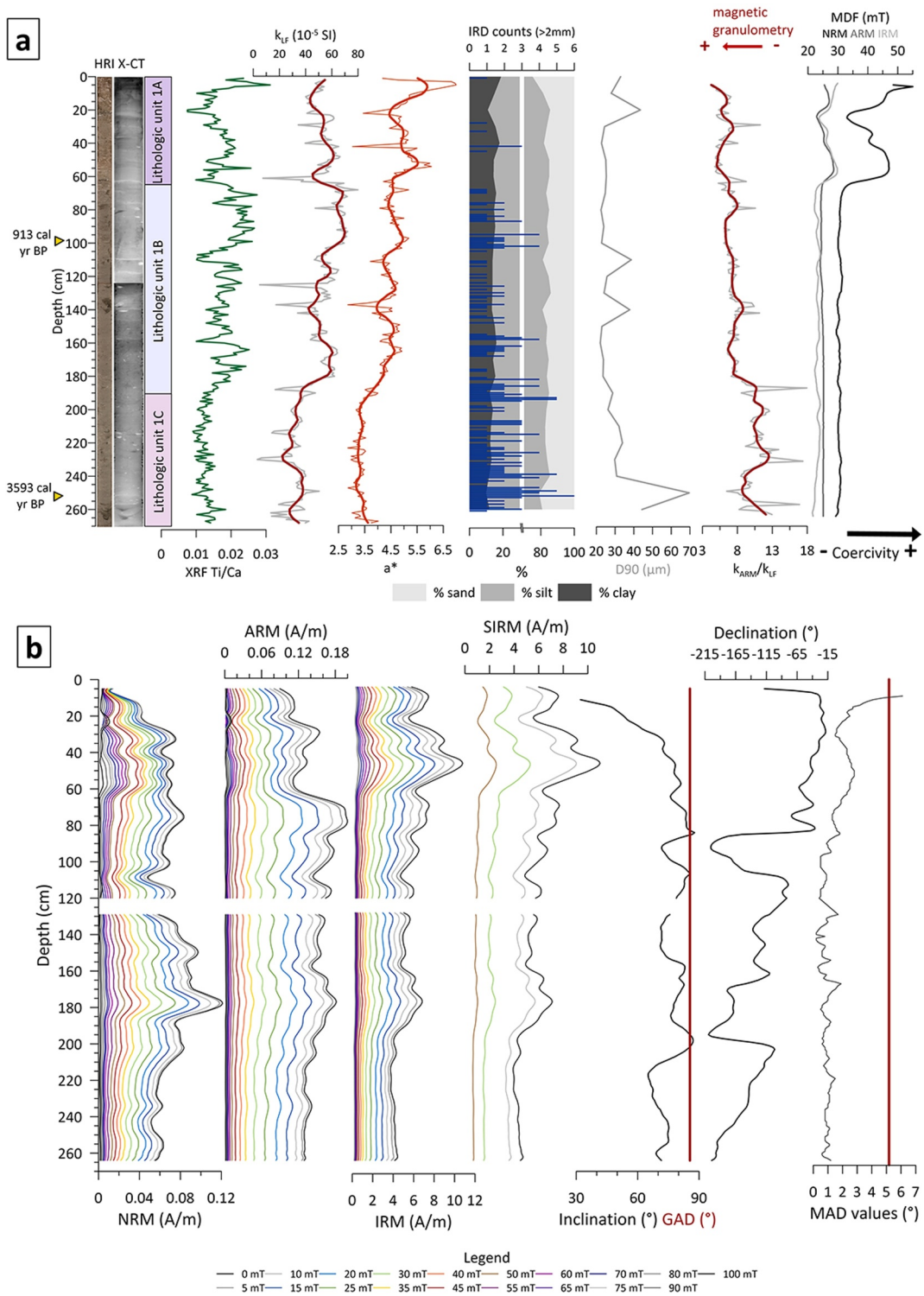

Figure 2. (a) Downcore physical and magnetic properties in core AMD1902-10GC including: high-resolution core image (HRI), X-ray computed tomography (X-CT) scan image, Ti/Ca profile, magnetic susceptibility (k_{LF}), a* red color indicator, relative abundance of the sand, silt and clay, ice rafted debris (IRD) counts based on X-CT images (>2 mm clasts), grain size proxy D90 (um), k_{ARM}/k_{LF} (magnetic grain size proxy), Median Destructive Field values (mT) of natural remanent magnetization (NRM), anhysteretic remanent magnetization (ARM) and isothermal remanent magnetization (IRM) (magnetic mineralogy indicator). (b) Downcore continuous paleomagnetic measurements of core AMD1902-10GC including demagnetization steps 0–100 mT, NRM (A/m), ARM (A/m), IRM 300 mT (A/m), saturation isothermal remanent magnetization (SIRM) 950 mT (A/m), characteristic remanent magnetization (ChRM) Inclination (°) and GAD value, ChRM relative Declination (°) and maximum angular deviation (MAD) values (°).

- 190–270 cm: light gray clay, high IRD content, stable Ti/Ca (0.01–0.02), lower k_{LF} (20–40 · 10^{-5} SI) and a* (3.5), stable MDF close to 30 mT, higher k_{ARM}/k_{LF} (8–18).

This is coherent with units 1A, 1B, and 1C described in previous studies in Petermann Fjord (Jennings et al., 2022; Reilly et al., 2019). As in Reilly et al. (2019), unit 1A refers to the unit from 0 to 65 cm, 1B from 65 to 190 cm and 1C from 190 to 270 cm.

It is possible that a coercivity transition between units 1A and 1B is related to an oxidic/suboxidic transition. Above this redox change, magnetite could have undergone changes such as maghemitization or maghemite coating. However, in 10GC, redox sensitive elements such as Mn and Fe do not display the variations expected at the redox boundary (Froelich et al., 1979, Figure S1 in Supporting Information S1), such as layers with peaks in Mn concentrations or down core changes in Fe concentration. Moreover, Al, which is redox independent, demonstrates an increase in the top 55 cm of core 10GC associated with the lithologic transition. Due to over penetration, the top of 10GC was lost during coring, whereas 04GC (Reilly et al., 2019) has a good recovery of the surface and shows a Mn peak at ∼30 cm. This may indicate that redox could still explain this coercivity shift in 10GC, although we cannot fully rule out that the coercivity change may be associated with a provenance change related to the presence of the ice tongue. Similar magnetic mineralogic changes were observed in studies of southern Greenland with no discernible impact on the paleomagnetic signal (Stoner et al., 1995, 2013).

NRM, ARM, IRM and SIRM are characterized by a strong and stable magnetization (Figure 2b). The sediment is well demagnetized and exhibits a generally stable single component magnetization (Figure S2 in Supporting Information S1) except for an intensity increase for the 75–100 mT AF demagnetization steps at ∼25 cm, which is sometimes observed during AF demagnetization (Hu et al., 1998). This magnetization was acquired parallel to the last applied field (z axis), which could reflect a spurious ARM and rule out a gyroremanent magnetization. MAD values are <5°, indicating a well resolved magnetization, and inclination values vary around the Geoentric Axial Dipole value (GAD; Figure 2b), indicating high quality directional data and reliable inclination and declination results. NRM directions are less well defined at the top of core (MAD > 5°, low inclination values), likely reflecting a coring disturbance (Montero-Serrano & Brossard, 2019). ARM values are lower at the top of the core (0–65 cm) than for the rest of the core, whereas IRM values are higher for that part of the core than for the rest of the core. Along with higher MDF values (Figure 2a), this further supports inferences of a change in magnetic minerals. The interval 70–180 cm demonstrates more variations in NRM, ARM, IRM and SIRM values than the interval 180–250 cm where the values are much more linear.

3.3. Magnetic Assemblage

The results of the discrete magnetic analyses are presented in Figure 3. Temperature-dependent magnetic susceptibility measurements demonstrated, on all heating curves, a clear Curie transition around 580°C, indicating the presence of magnetite in the samples (Figure 3a). To precisely determine the temperature of the transition, curve derivatives were calculated. Curie temperatures ranged from 571 to 596°C. Magnetic susceptibility drops shortly before 580°C for samples 25, 40, and 180 and significant magnetic susceptibility persists beyond 600°C, indicating the possible presence of hematite. The sample at 40 cm shows an increase in susceptibility starting around 450°C with a maximum of 525°C. Similar but smaller peaks are also present in samples at 10, 25, 50, and 130 cm. A slight bump at 300°C is visible in the heating curves of the samples at 10, 40, and 130 cm and less but still visible in a sample at 180 cm, suggesting the presence of titanomagnetite. All samples are characterized by an increase in susceptibility after cooling, indicating an increase in the magnetite content.

The shapes of the hysteresis loops (Figure 3b) are typical of low coercivity minerals such as magnetite or titanomagnetite (e.g., Tauxe et al., 1996). However, hysteresis loops are not totally linear at 300 mT and reach saturation between 0.5 and 1 T (Figure 3b), indicating the presence of higher coercivity minerals, despite the dominance of magnetite. This is supported by the S-ratio values (Bloemendal et al., 1988; Table 3). According to the hysteresis loops, all magnetization values were multiplied by a factor 10 after heating (Figure 3b). Magnetization of samples at 25 and 40 cm increased slightly less (0.058–0.3; 0.058–0.4), contrary to the sample at 250 cm for example, (0.02–0.2). Mrs and Ms values are higher after heating except for the sample at 10 cm (Table 3). Multiplication factors were slightly higher for Mrs than for Ms (Table 4).

On IRM acquisition curves and unmixing diagrams (Figure 3c), top samples (10 and 40 cm) demonstrate major coercivity component at 66.6 and 64.6 mT, whereas bottom samples (130 and 250 cm) show major coercivity

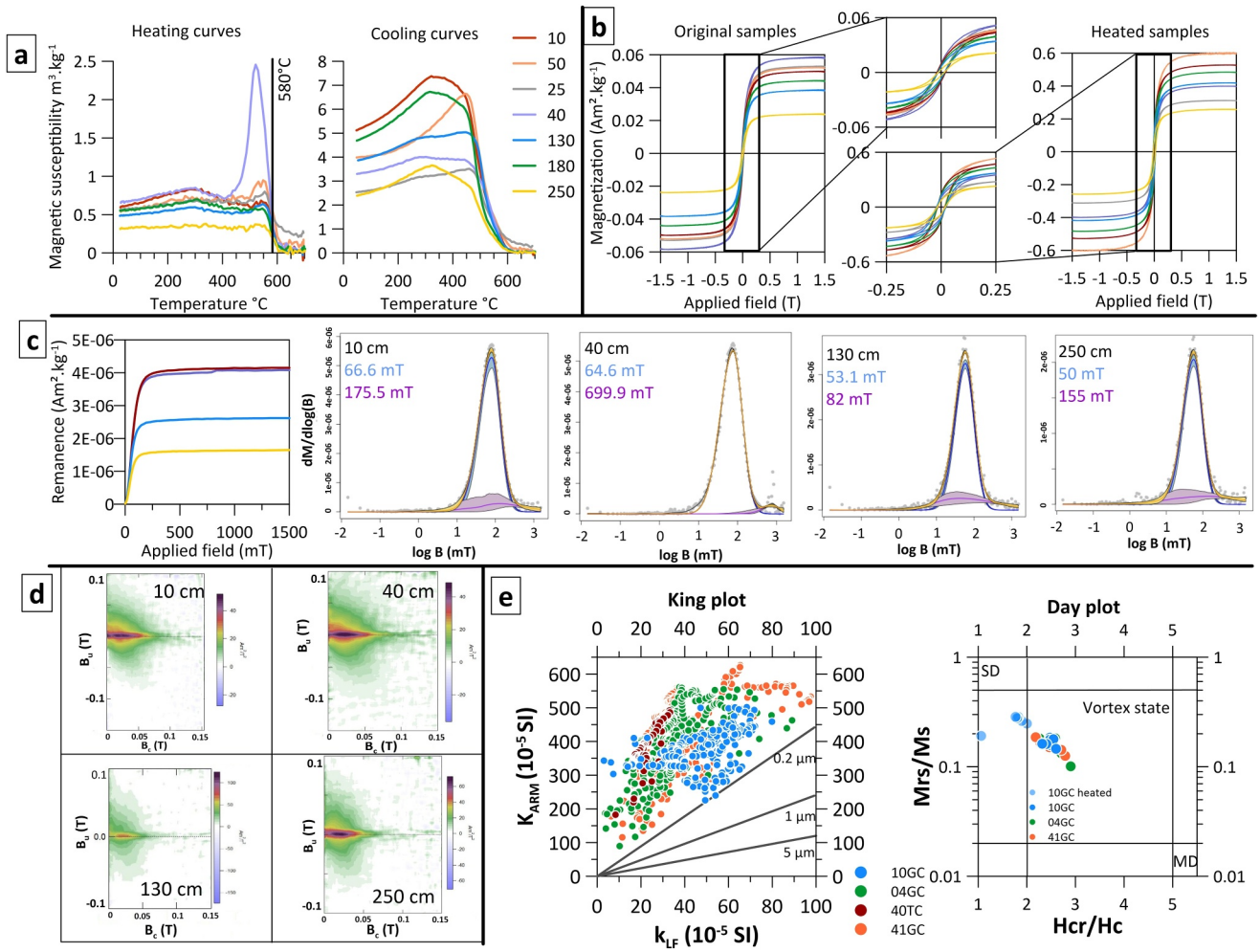

Figure 3. Rock magnetic analysis results. (a) Magnetic susceptibility heating and cooling thermomagnetic curves. (b) Hysteresis loops of samples before and after heating to 700°C. (c) Isothermal remanent magnetization (IRM) acquisition curves and IRM unmixing. (d) FORC diagrams. (e) Day & King plots.

component at 53.1 and 50 mT, indicating the influence of higher coercivity minerals in the top of the core. All samples illustrate the contribution of a high coercivity component, more pronounced in the 40 cm sample. S-ratio (Table 3) is comprised between 0.97 and 0.98 for the seven samples, indicating that magnetite dominates the magnetic signal despite the presence of high coercivity minerals.

FORC diagrams (Figure 3d) reveal peak central ridges >40 Am^2/T^2 between 0.01 and 0.05 T (Bc) for samples 10 and 40, and >60 Am^2/T^2 between 0.005 and 0.03 T for samples at 130 and 250 cm, characteristic of Pseudo single domain magnetite (PSD) magnetite. Sample 130 is characterized by a strong central positive ridge around the axis Bu = 0 with a main positive peak Bc ~0.03, which is characteristic of single domain (SD) particle behavior with low magnetostatic interactions between particles. This sample does not reveal stretching along the negative Bu axis, which would be a sign of superparamagnetic (SP) particles, and low magnetization in the vortex state and multi domain (MD) areas, confirming the dominance of SD particles in that sample. Samples at 10 and 40 cm are very similar and depict strong positive central ridges as well as a strong magnetization close to the 0 axis and a low magnetization in the vortex state. This enables us to assess the large dominance of SD particles with few interactions and with the probable presence of some MD and vortex states particles, but almost no SP particles, in both samples. Again, in the sample at 250 cm, the central ridge indicates that most particles are SD with some interactions; the lobes indicate vortex state particles, and the low magnetization values along the Bu axis indicate almost no MD and SP particles. Overall, the four samples have the characteristics of noninteracting SD detrital magnetite.

Table 3
Hysteresis and S-Ratio Measurement Results (Heated Samples in Gray)

	Mrs	Ms	Hc	Hcr	IRM −300 mT	SIRM	S-ratio (Bloemendal et al., 1988)
10 cm	9.14E−03	4.96E−02	1.95E−02	4.83E−02	−3.74E−06	3.92E−06	0.9780
25 cm	8.26E−03	5.27E−02	1.60E−02	3.97E−02	−3.16E−06	3.31E−06	0.9779
40 cm	1.02E−02	5.79E−02	1.87E−02	4.61E−02	−3.72E−06	3.88E−06	0.9790
50 cm	9.27E−03	5.18E−02	1.93E−02	4.92E−02	−3.51E−06	3.65E−06	0.9807
130 cm	6.15E−03	3.81E−02	1.53E−02	3.68E−02	−2.32E−06	2.46E−06	0.9719
180 cm	7.10E−03	4.38E−02	1.60E−02	3.71E−02	−2.64E−06	2.78E−06	0.9756
250 cm	3.44E−03	2.36E−02	1.38E−02	3.58E−02	−1.48E−06	1.57E−06	0.9694
10 cm	2.52E−05	9.18E−05	1.82E−02	3.31E−02	−24.13E−06	2.40E−05	1.0018
25 cm	7.70E−02	3.11E−01	1.93E−02	3.86E−02	−8.876E−06	8.78E−06	1.0050
40 cm	1.04E−01	3.98E−01	2.20E−02	4.19E−02	−1.35E−05	1.35E−05	1.0000
50 cm	1.14E−01	5.97E−01	1.46E−02	1.55E−02	−3.70E−06	2.78E−06	1.1660
130 cm	1.19E−01	4.17E−01	2.08E−02	3.80E−02	−1.94E−05	1.94E−05	1.0012
180 cm	1.34E−01	4.82E−01	1.82E−02	3.28E−02	−1.74E−05	1.73E−05	1.0040
250 cm	7.35E−02	2.57E−01	1.92E−02	3.40E−02	−1.01E−05	9.99E−06	1.0031

All samples on the King plot (King et al., 1983; Figure 3e) are located above the theoretical 0.2 μm limit, indicating small grains within the same core and between the four cores composing the stack, although magnetic susceptibility measurements were conducted on whole cores for cores 41GC, 04GC, and 40TC and split core for core 10GC. On a modified Day plot (Day et al., 1977; Figure 3e), samples are all located within the vortex state range (Roberts et al., 2017) equivalent to the PSD (Dunlop, 2002), supporting the FORC results and confirming the relatively homogeneous magnetic grain size. All samples show lower Hcr/Hc after heating, indicating that the average population of grains is finer.

In summary, core 10GC (except for the top 70 cm) falls within the criteria for sediments likely to preserve past variation in RPI (King et al., 1983; Tauxe, 1993): the magnetic signal is strong and stable (MAD < 5°) and carried by low coercivity grains such as magnetite and/or titanomagnetite; the magnetic grain size falls within the SD and vortex state; the NRM, ARM, and IRM intensity variations are inferior to an order of magnitude; and finally, the inclination values vary around the GAD.

3.4. RPI Determination

The best normalizer (ARM or IRM) for RPI for core 10GC (Figure 4) was determined using both the slope (Tauxe et al., 1995; Valet & Meynadier, 1998) and ratio methods (Channell et al., 2000; Stoner et al., 2000; Tauxe & Wu, 1990). Both methods render similar results for both normalizers for the 71–265 cm interval and results that differ for the top 70 cm. The correlation coefficient (r^2) between the normalized signal and the normalizer was calculated for both ARM and IRM for the ratio method. r^2 values are non-significant but lower for the ARM than

Table 4
Factors of Multiplication Describing Magnetic Changes in Hysteresis Parameters After Heating

	Mrs	Ms	Hc	Hcr	IRM −300 mT	SIRM	S-ratio (Bloemendal et al., 1988)
10 cm	0.0028	0.0019	0.9333	0.6853	6.4519	6.1224	1.0243
25 cm	9.3220	5.9013	1.2063	0.9723	2.8089	2.6526	1.0277
40 cm	10.1961	6.8739	1.1765	0.9089	3.6290	3.4794	1.0215
50 cm	12.2977	11.5251	0.7565	0.3150	1.0541	0.7616	1.1889
130 cm	19.3496	10.9449	1.3595	1.0326	8.3621	7.8862	1.0301
180 cm	18.8732	11.0046	1.1375	0.8841	6.5909	6.2230	1.0291
250 cm	21.3663	10.8898	1.3913	0.9497	6.8243	6.3631	1.0348

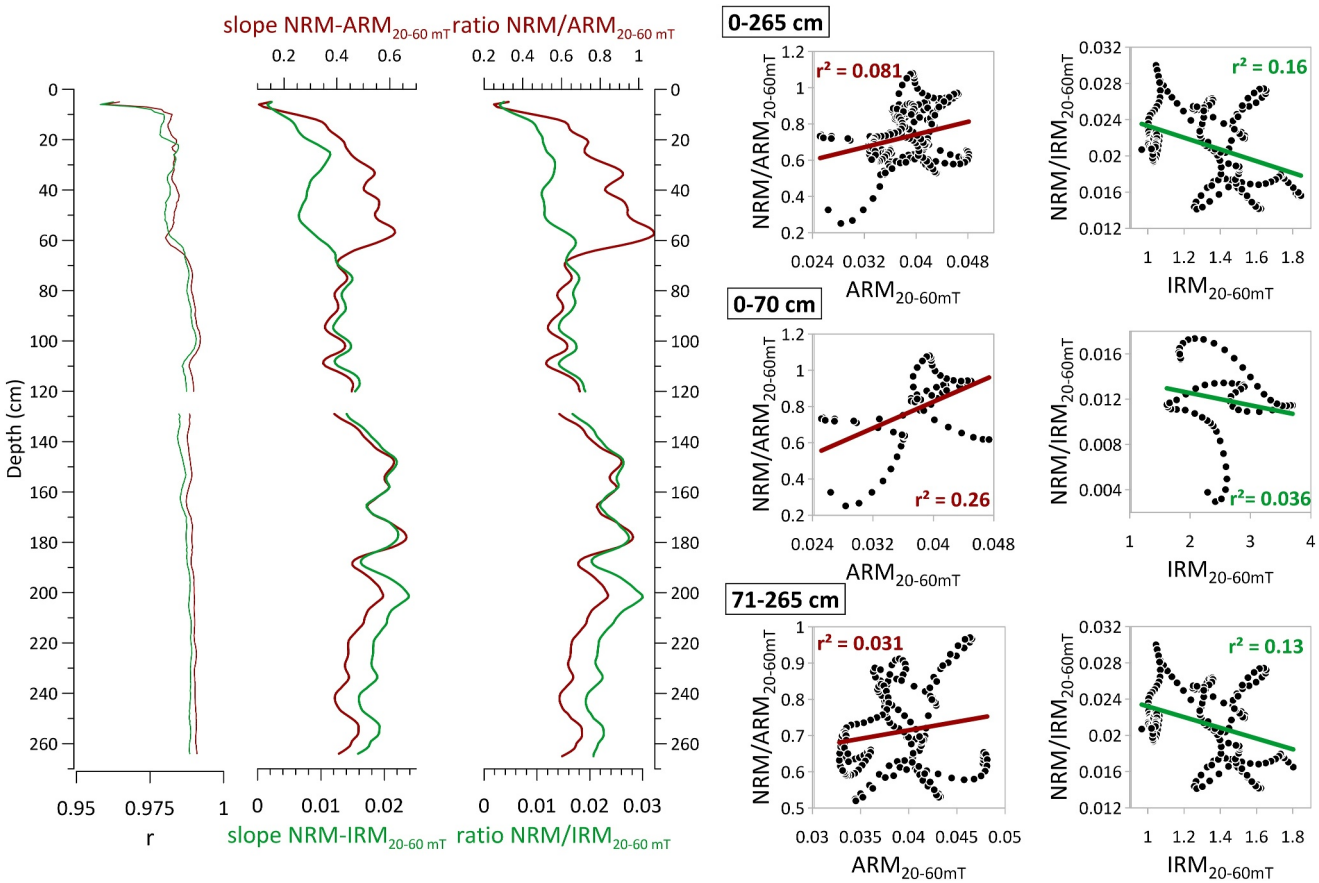

Figure 4. Determination of the 10GC relative paleointensity signal (20–60 mT). *R*: correlation coefficient for anhysteretic remanent magnetization (ARM) (red) and isothermal remanent magnetization (IRM) (green); profiles for slope method; profiles for ratio method. Determination coefficient r^2 between the normalized signal and the normalizer for ARM (red) and IRM (green) for the whole core, core top (0–70 cm) and core bottom (71–265 cm).

for the IRM for the whole core. Given the differences in mineralogy above and below 70 cm, r^2 was calculated for both intervals separately. For the top 70 cm, r^2 is lower for IRM than for ARM, contrary to the rest of the core where r^2 is lower for ARM than for IRM. r^2 calculated for the slope method is superior to 0.98 for 71–265 cm and comprised between 0.96 and 0.98 for the top 70 cm. ARM seems to be a better normalizer for the whole core except for the top 70 cm, but because of the uncertainty of that interval regarding RPI reliable recording, we decided not to take it into account and chose ARM as our preferred normalizer. Moreover, the slope method with ARM showed better agreement between the four cores than the slope method using IRM, and ARM shows lower r^2 with the ratio method for the four cores (Figure S4 in Supporting Information S1).

The normalized intensity derived from the slope method will be used hereafter in the stacking process and comparisons. Because of the similarity between the slope and ratio methods with both ARM and IRM, the core 10GC normalized intensity signal from 71 to 265 cm interval seems robust. Precaution should be taken when interpreting the normalized intensity for the top of the core (0–70 cm) because of the different magnetic mineralogy and differences between the 2 normalizers for the same method and differences between the 2 methods for the same normalizer. It is also the interval where the difference between the signals of the four cores is the largest (Figure 6). The discrepancy in the normalizers shows that the use of the same normalizer for the whole core cannot represent RPI very well when there are significant mineralogy variations throughout the core. However, because of the stacking process, it was important to keep consistency in the normalizers between the different cores, and we consider that it only affects the top part of the stack (0–70 cm).

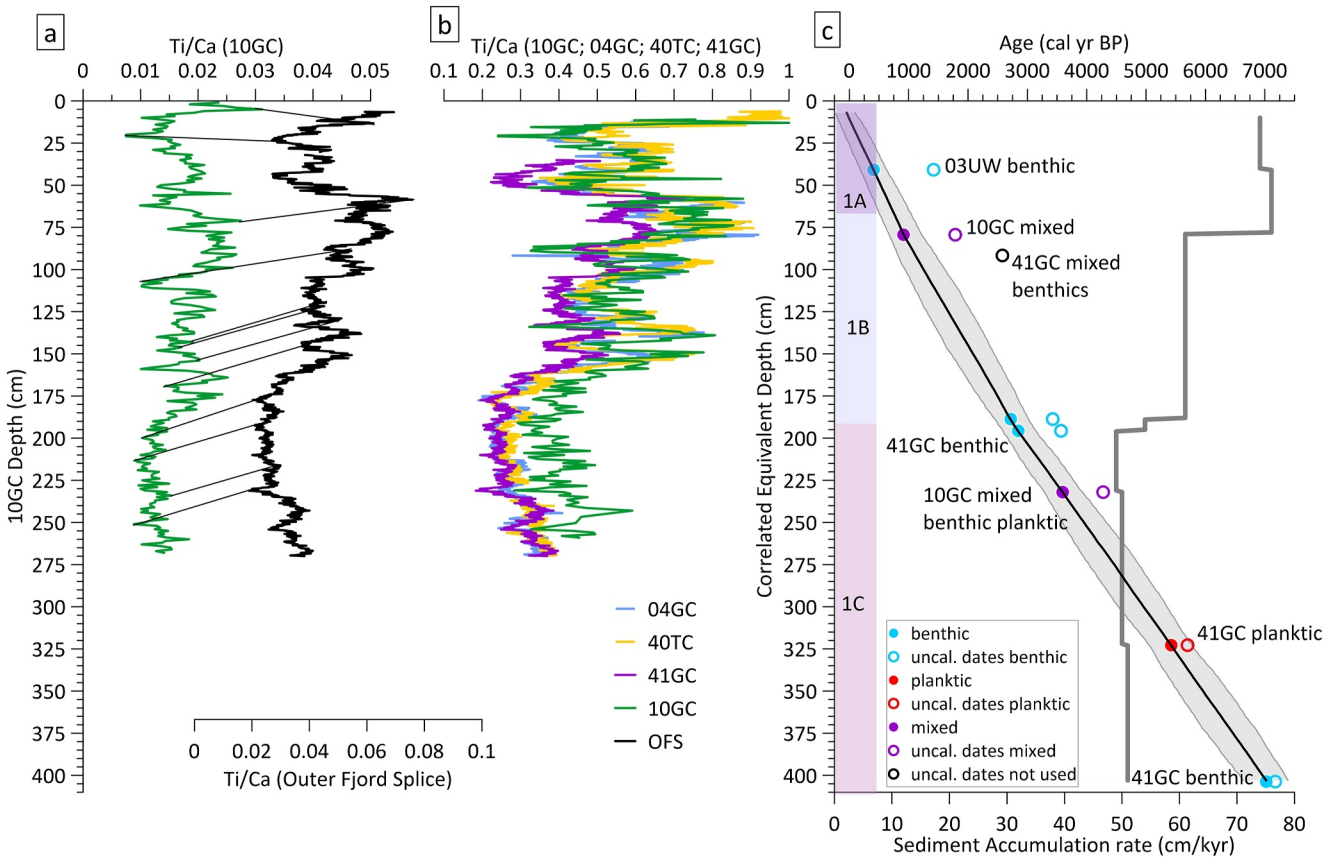

Figure 5. (a) Conversion of 10GC (independent depth, cm) to the Correlated Equivalent Depth (CED, cm) using Ti/Ca X-ray fluorescence (XRF) ratio from the outer fjord splice (OFS; 03PC, 03TC, 41GC). (b) Comparison of Ti/Ca XRF ratio of the four cores composing the stack (04GC, 41GC, 04TC, 10GC) on CED. (c) Age model and accumulation rates for Petermann stack using ^{14}C dates from cores 41GC, 03UW (Reilly et al., 2019) and 10GC (this study), Marine 20 calibration curve and $\Delta R = 430 \pm 145$ years. Red = planktic foraminifera, blue = benthic foraminifera, purple = mixed benthic and planktic, black = uncalibrated dates, white = date not used in the age model.

3.5. Paleomagnetic Stack

In Petermann Fjord, the Outer Fjord Splice (OFS) composed of three cores (40GC, 03PC, 03TC) places all the cores on a common depth scale, here called the Correlated Equivalent Depth (CED; Reilly et al., 2019). Using pXRF data, QAnalySeries software (QAS; Kotov & Pälike, 2018) was used to obtain the best fit between cores 10GC and the OFS. Because the cores were not measured with the same instrument, the Ti/Ca ratios were standardized using the mean and standard deviation on the depth interval 0–270 cm. This interval was chosen because of the length of core 10GC and the larger amplitude variations of the XRF signal at the bottom of the other cores. All cores being on the same depth scale are required for the stacking process. Correlation coefficients were calculated with QAS between all the Ti/Ca profiles (10GC, 40TC, 04GC, and 41GC) two by two (Table S4 in Supporting Information S1).

PSV and RPI stacks were constructed following the approach of Reilly et al. (2018, 2019). Bin widths of 5 cm CED were used to calculate the Fisher mean of the directions (Fisher, 1953) with N being the number of cores contributing to the stack for each calculation, rather than the number of measurements in each bin. MAD values were converted to α_{95} following Khokhlov and Hulot (2016) and the uncertainty was propagated in the stacking process through 1,000 random sampling of the α_{95} distributions. Core 10GC declination values were rotated by 45° to match the declination of the previously created stack of the three other cores. Uncertainty was propagated suggesting a circular distribution on a sphere.

Core 10GC depth conversion to the CED is presented in Figure 5 and stacking results are in Figure 6. Core 10GC Ti/Ca profile presents a r^2 of 0.75 with the OFS Ti/Ca signal, and the Ti/Ca signals of the four cores on the same depth

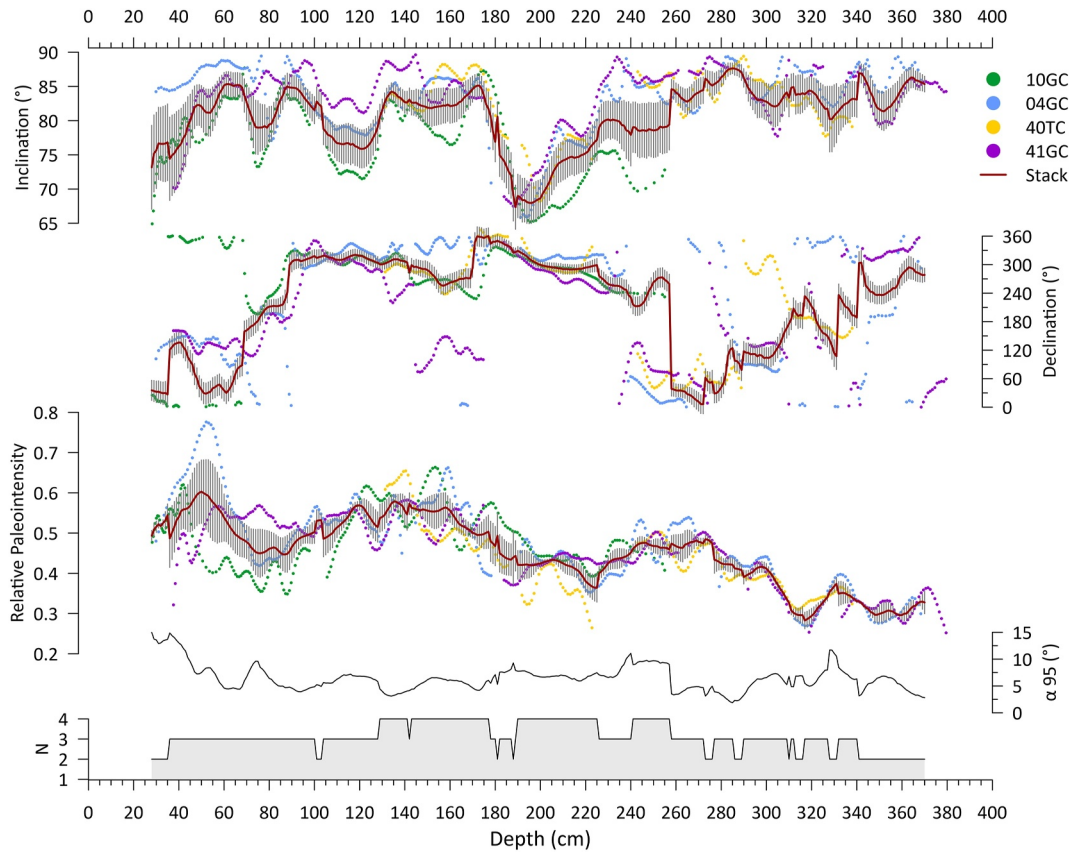

Figure 6. Petermann paleomagnetic secular variations stack: inclination, declination, relative paleointensity (RPI), angular difference (α95) and number of cores contributing to the stack (N).

scale present correlation coefficients with each other varying between 0.69 and 0.94 (Figure 5b). The number of cores contributing to the stack is always >2, with the signal being the most reliable when four cores are contributing between 130 and 260 cm. All cores display similar variations. Core 10GC has the lowest value for the inclination record. The inclination displays high values >65° for the whole stack and >80° for several parts of the stack. At a very steep inclination, a small angular change can lead to large changes in declination (Reilly et al., 2019), explaining the large variability of the declination values. The declination values are therefore likely to be more reliable for the intervals where the inclination is shallower. Based on that assumption, we rotated the declination of core 10GC according to the other cores at the shallowest inclination intervals (~190 cm), that is, by 45°. Prior to stacking, 10GC declinations values were also aligned between sections to avoid abrupt shifts at core section limits. For cores 40TC, 04GC, and 41GC, all sections were split along the same plane. In Figure 6, declination values are presented in a 0–360° range, so another 360° was added to core 10GC declination values to keep the variation amplitude between 0 and 360° and to compensate for the lack of azimuthal orientation. The low inclination at 190 cm is the most prominent feature and is well observed in the four cores. Moreover, the inclination variations in 10GC confirm the presence of two inclination features at 80 and 120 cm. Core 10GC inclination values are lower than the other cores in the intervals 190–220 cm and 240–260 cm. To minimize that difference, other XRF profile correlations were tried. Nonetheless, the initial correlation on the depth scale using the XRF profiles was used for several reasons: the correlation coefficient between the XRF profiles was higher, the alignment of the uncalibrated ages was the most linear (Figure S5 in Supporting Information S1) and more importantly, to keep the chronology independent of paleomagnetism at this point (would not have been the case with k_{LF} or PSV).

3.6. Age Model

The age model is presented in Figure 5. According to the proposed age model, the core 10GC spans the last 5 kyr, and the stack spans the last 7 kyr. Adding core 10GC to the previous stack (Reilly et al., 2019) reinforced the age

model by adding two more ^{14}C dates (Figure 5). More precisely, it enabled us to refine the 200–320 cm (CED) interval, where ages were lacking, with the 10GC date (AWI#10208.1.1). Moreover, the addition of the 10GC age AWI#10207.1.1 justified the exclusion of the 41GC age ANU#17240. Indeed, that sample was considered too old because of its offset relative to a linear age-depth relationship. For that sample, the uncalibrated age only is presented in Figure 5. The other ages are presented and discussed in Reilly et al. (2019). SAR in Petermann Fjord was calculated using the calibrated ages of the four cores on the CED and indicated three depth intervals of different SAR that correspond broadly to the three lithologic units: 75 cm/ka (0–80 cm), 60 cm/ka (80–190 cm), and 50 cm/ka (190–400 cm). SAR transitions are based on where the radiocarbon dates are located, which is likely an artifact and SAR changes more likely occurred at the lithologic boundaries.

3.7. PSV Variations

To facilitate further comparisons with records from outside the Petermann Fjord, PSV from previously published records, all projected to the location of Petermann Fjord via their VGP paths (precise coordinates of 10GC), are displayed in Figures 7 and 8. Similar peaks and lows of inclination, declination and RPI can be seen in the different models and records. The records were chosen based on their location (Arctic, Northern Europe, northern North Atlantic, inside and outside of the TC projection surface) and their SAR and resolution (same order of magnitude as the Petermann stack). CALS10k.2 (Constable et al., 2016) and ARCH3k.1 (Donadini et al., 2009) data were obtained from the GEOMAGIA database (Brown et al., 2015).

The Petermann Fjord inclination stack shows good agreement with U1305 (Southern Greenland; Stoner et al., 2013), GREENICE (east Greenland-Iceland; Stoner et al., 2007), JPC15 (Chuckchi Sea; Lund et al., 2016) and core 204 from Baffin Bay (Caron et al., 2019) inclination record, although the shallow inclination feature at ~2.5 ka appears earlier in that record that could be consistent with age model uncertainty. Comparison with the recent global data model outputs pfm9k.2 model signals (Nilsson et al., 2022; Figure 8a) also shows significant similarities. In contrast, records like MD99-2220 from the St. Lawrence Estuary (St-Onge et al., 2003) and those from Northern Europe are fundamentally different. The shallow inclination feature is more pronounced as well at the coordinates of Petermann Fjord than at the original coordinates of the records (e.g., GREENICE; Reilly et al., 2023; Stoner et al., 2007). The Petermann PSV stack, JPC15 Chukchi Sea record (Lund et al., 2016), and Baffin Bay record (Caron et al., 2019) are all located within the TC surface projection (70°N) but display variations similar to the records situated outside (U1305, GREENICE, north Karelian stack, Eastern Canadian stack, Lake le Boeuf). Inclination variations in the St-Lawrence Estuary (Barletta, St-Onge, Stoner, et al., 2010) at lower latitudes are similar to the variations in Northern Europe (North Karelian stack) but with a slight temporal offset. Similarities in the inclination variations can be observed between U1305, GREENICE, JPC15 and Petermann stack even though they are not all situated within the TC surface projection. The Petermann declination stack has similarities with other regional Arctic records, similar to inclination, though it is more subdued than those sites transferred to the Petermann location. The Petermann stack shows inclination similarity with the pfm9k.2 model with common key features at 1, 3.7, and 6 ka (underlined in Figure 7). The Petermann stack declination shows a decrease at 2.5 ka, which can be identified in the pfm9k.2 model, U1305, GREENICE and the North Karelian stack (Finland; Haltia-Hovi et al., 2010) and another decrease at 4.5 ka, which is less clear in individual Petermann records (Figure 6) and at other locations.

Comparison of paleointensity records shows that high intensities are observed at 0.8–1.2 ka (Eastern Canadian Stack ECS, Western Europe, U1305, models pfm9k.2 and CALS10k.2), 1.3–2.2 ka (Petermann stack, CALS10k.2, pfm9k.2, U1305) and 2–2.4 ka (Lake LeBoeuf, Western Europe, U1305, CALS10k.2, pfm9k.2). Low intensities are identified by other records for the same intervals: 0.8–1.2 ka (Petermann stack, Lake LeBoeuf, AMD2014-204casq), 1.3–2.2 ka (Western Europe, ECS, Lake LeBoeuf, AMD2014-204casq), 2–2.4 ka (Petermann stack), 4.8–5.3 ka (Petermann stack, CALS10k.2, pfm9k.2).

Correlation coefficient was calculated between the Petermann stack RPI signal and other records using the QAS software (Supporting Information S1). The Petermann RPI signal (Figure 8) has a higher correlation coefficient with the pfm9k.2 model (0.76) than with the CALS10k.2 model (0.57). It is interesting to underline that the RPI record from U1305 has a higher correlation coefficient (0.77) with paleointensity (Virtual Axial Dipole Moment [VADM]) from European archeomagnetic data (VADM western Eurasia; Genevey et al., 2008) than with the Petermann RPI stack (0.68 for the median age, 0.287 for the min age and 0.612 for the max age).

10.1029/2024GC011620

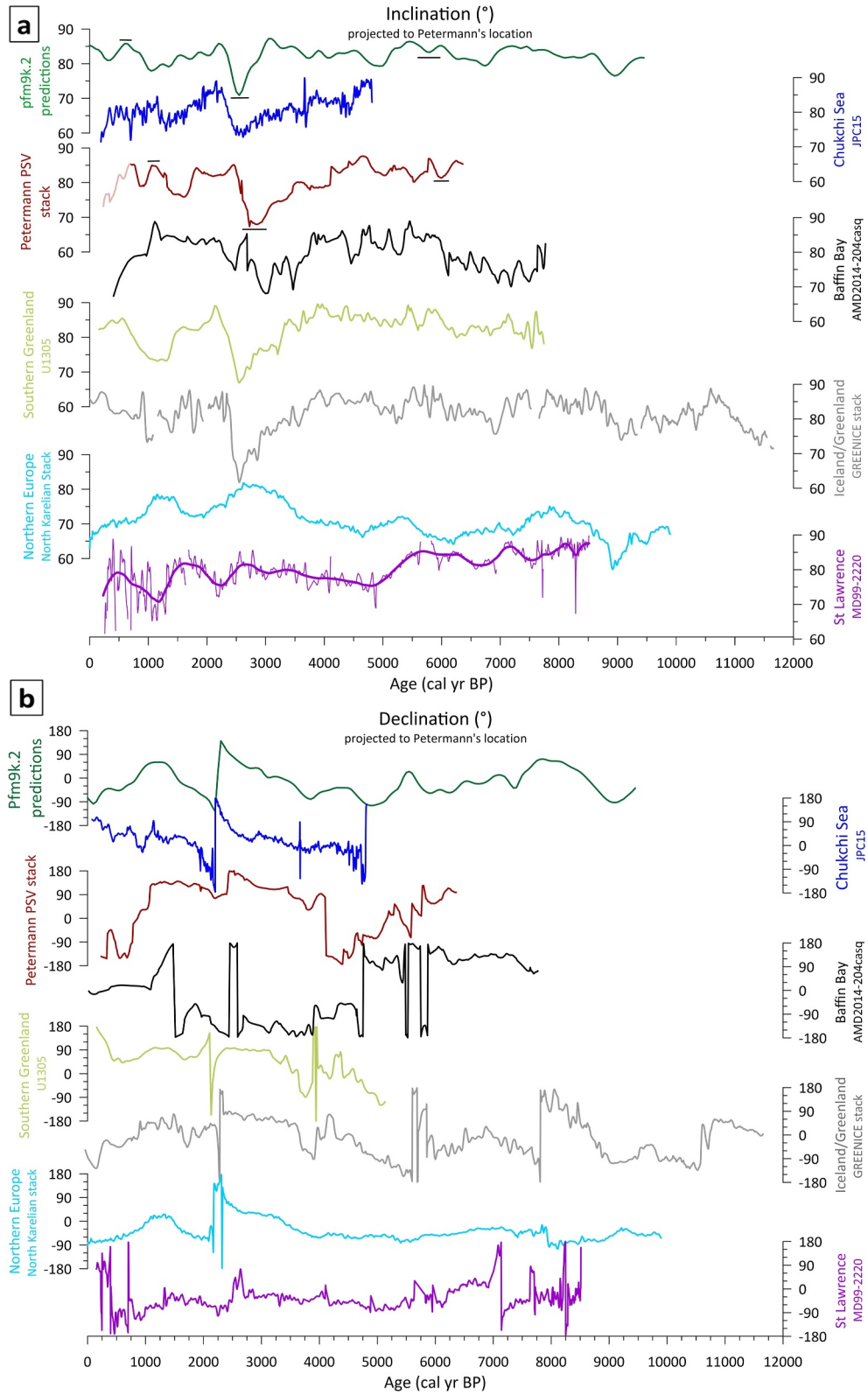

Figure 7. Comparison of inclination (a) and declination (b) profiles from different paleorecords: pfm9k.2 geomagnetic model (Nilsson et al., 2022), JPC15 (Lund et al., 2016), Petermann stack (this study), 204casq (Caron et al., 2019), U1305 (Stoner et al., 2013), GREENICE stack (Stoner et al., 2007), North Karelian stack (Haltia-Hovi et al., 2010), MD99-2220 (St-Onge et al., 2003). Key features (1, 3.7, and 6 ka) mentioned in the text are underlined in the figure.

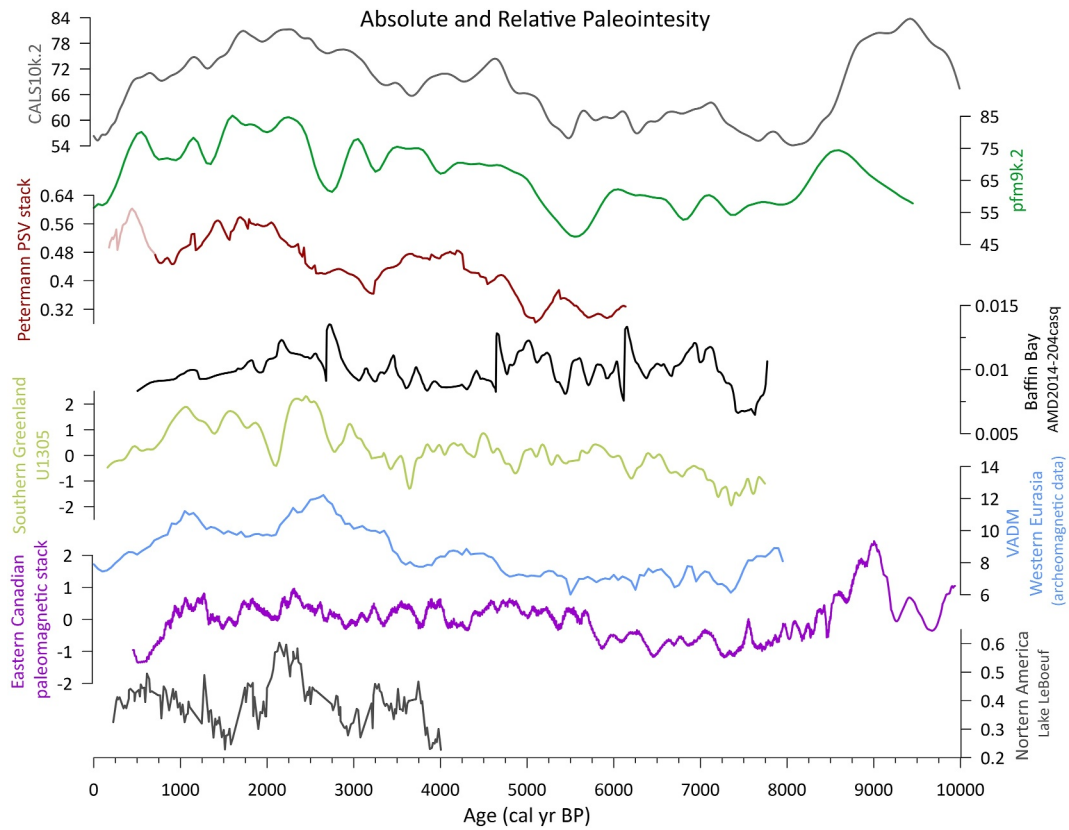

Figure 8. Comparison of absolute and relative paleointensities profiles for different paleorecords: CALS10k.2 (Constable et al., 2016) and pfm9k.2 geomagnetic models (Nilsson et al., 2022), Petermann stack (this study), 204casq (Baffin Bay relative paleointensity (RPI) record, Caron et al., 2019), U1305 (North Atlantic RPI record, Stoner et al., 2013), GREENICE stack (Northern North Atlantic RPI record, Stoner et al., 2007), North Karelian stack (lacustrine RPI record from Finnish lakes, Haltia-Hovi et al., 2010), Virtual Axial Dipole Moment, Western Eurasia (absolute paleointensity from archeological artifacts and volcanic products; Genevey et al., 2008), Eastern Canadian stack (St-Lawrence RPI record, Barletta, Channell, & Rochon, 2010), Lake LeBoeuf (lacustrine RPI record from North America, King et al., 1983).

4. Discussion

4.1. Age Model, Magnetic Lock-In Depth and Δ*R* Variations

While there are broad similarities in the comparisons discussed in Section 3.6, we notice a systematic offset relative to the better understood chronologies of the region around Iceland (Hagen et al., 2020; Reilly et al., 2023; Stoner et al., 2007, 2013). For example, the Petermann Fjord record is systematically slightly older than the GREENICE record, which could be explained by either lock-in depth uncertainty or an underestimated Δ*R* (Figure 9).

In order to evaluate potential Δ*R* variation or magnetic lock-in depth, paleomagnetic tie points were chosen from the Petermann stack in comparison with the GREENICE stack (Stoner et al., 2013) to calculate the age of the magnetization. GREENICE was constructed with a large number of ^{14}C ages (44) and tephras and depicted very high SAR (>1 m/ka, up to 5 m/ka; Stoner et al., 2007). With such a high SAR, the temporal offset associated with any lock-in depth is probably very small (Reilly et al., 2023). The selected tie points (Table 5) were used to calculate the mean depth offset between the 2 curves, which was evaluated at 11 ± 3.6 cm and could be considered an estimate of the lock-in depth offset at Petermann Fjord. This value is consistent with other estimates, such as the similarly derived 12 cm estimate for site U1305 (Hagen et al., 2020; Stoner et al., 2013) and the ~5–15 cm offset inferred from ^{10}Be data in lower accumulation rate cores (Simon et al., 2018; Suganuma et al., 2010). Using that value, the depth of the radiocarbon ages was adjusted (Table 5), and an updated age model was calculated to estimate the age of the magnetization (Figure 9b) following the approach of Stoner et al. (2013). The updated age

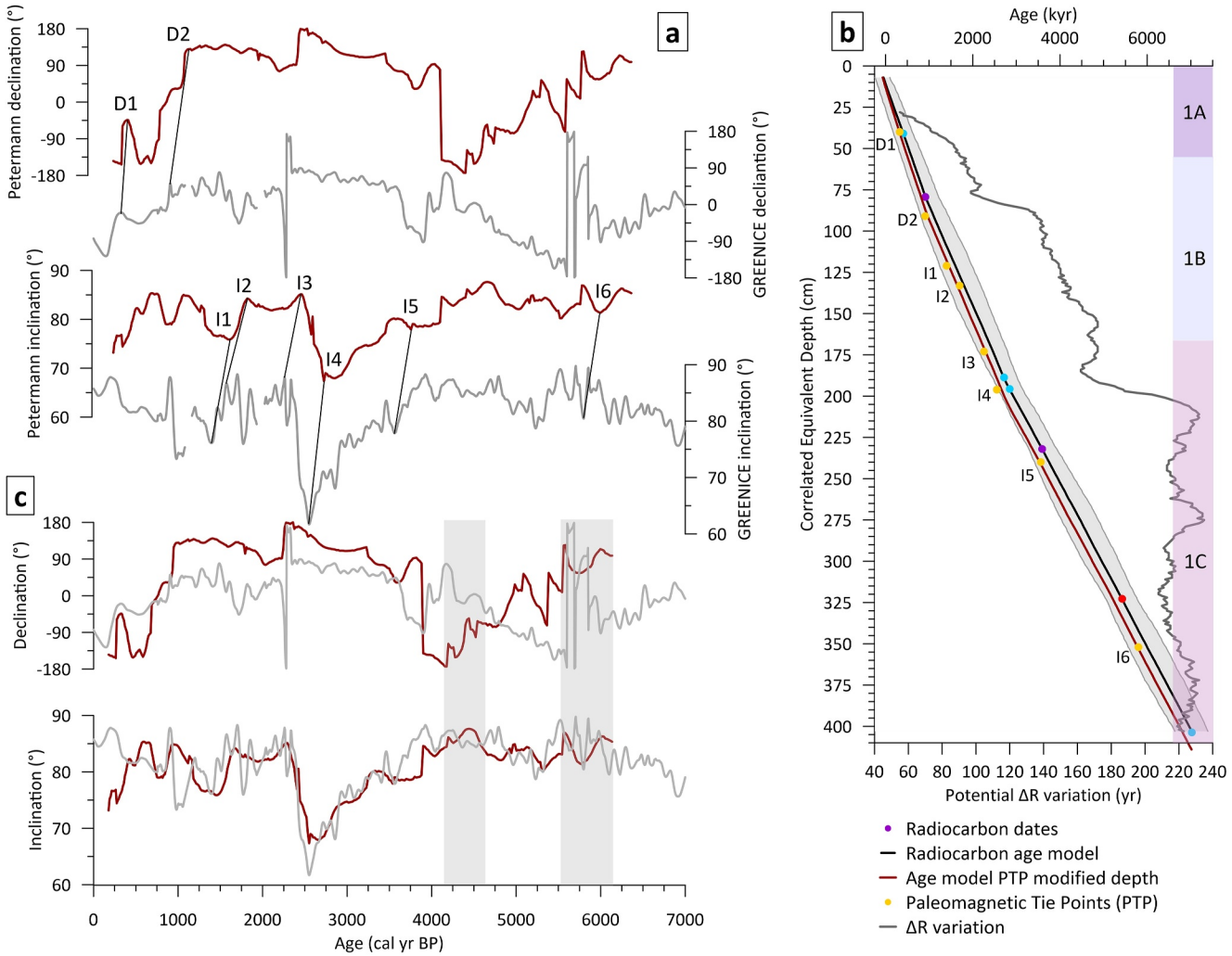

Figure 9. Construction of the magnetic age model for the Petermann stack. (a) Paleomagnetic tie points based on Petermann and GREENICE stack comparison. (b) Bayesian magnetic age-depth model for the Petermann stack. Yellow points = paleomagnetic tie points; red, blue, purple points = calibrated ^{14}C ages; red curve = magnetic age model; black curve radiocarbon age model; gray curve = Δ*R* variation. (c) GREENICE and Petermann Paleomagnetic Secular Variation stack comparisons based on the Bayesian magnetic age model. Gray shaded bars indicate inclination >85° where important declination changes should be interpreted carefully.

Table 5
Paleomagnetic Tie Points Used to Modify the Depth of the Radiocarbon Ages and to Calculate the Magnetic Age Depth Model

Tie point	Depth (cm)	Magnetic age (year BP) based on GREENICE	Depth ^{14}C (cm)	Depth offset (cm)
D1	40	325	35	−5
D2	91	910	79	−12
I1	121	1,400	109	−12
I2	133	1,700	127	−6
I3	173	2,260	160.5	−13
I4	196	2,555	179	−17
I5	240	3,560	230.5	−10
I6	352	5,800	342	−10

Table 6
Calculation of the Magnetic Depth for the Radiocarbon Ages for the Petermann Stack

Age (cal year BP)	CED (cm)	Magnetic depth (cm)
1,421	40.87	51.87
1,784	79.33	90.33
3,427	188.72	199.72
3,567	195.72	206.72
4,277	232	243
5,697	322.72	333.72
7,174	403.72	414.72

Note. The updated depths were used to construct the magnetic age model in the R package "rbacon".

model uses the same radiocarbon ages but with modified depth according to the offsets calculated in Tables 5 and 6.

An alternative explanation is that the offset between the magnetic age curve and the median radiocarbon age model actually represents uncertainty in the radiocarbon age model itself (specifically variation of the ΔR; Figure 9b). The age offset varies between 55 and 235 years, being lower at the top and higher toward the bottom of the core, with a mean of 181 years. The offset between the two curves is reasonable as the magnetic age curve is still comprised between the minimum and maximum of the initial age model, given the ± 145 ΔR uncertainty used (Figure 9). Variation of the reservoir age is a viable hypothesis given that calibration curves are challenging to use in the Arctic because of a number of factors, such as seasonal sea ice, mixing of water masses of different ages and meltwater inputs, among others (e.g., Pearce et al., 2023). Centennial scale uncertainty in ΔR is not unexpected in this environment as the built-in Marine20 calibration curve reservoir effect is not expected to reflect larger scale variability in the polar ocean (Heaton et al., 2020), and Petermann Fjord is known to have variability in sea ice and ice-tongue extents over this time interval (Detlef et al., 2021; Jennings et al., 2022; Reilly et al., 2019).

Previous studies introduced the hypothesis of the drift of the non-dipole field (Yukutake, 1967), that is, that the main geomagnetic field PSV features drift mainly westward (Dumberry & Finlay, 2007; Korte & Constable, 2018; Nilsson et al., 2020). Other studies found that the hypothesis and the previously published data were rather unconvincing (e.g., Tauxe, 2010). Here, we observe the features in GREENICE with a delay compared to the Petermann stack, located more to the west, which would run counter to the westward drift hypothesis. Moreover, the age offset between the two records is rather constant when the literature suggests variation in the drift rate (Nilsson et al., 2020). In addition, the observed features in the Petermann stack are then observed in the Chukchi Sea (JPC15 record) and in Southern Greenland (GREENICE record, U1305; Figure 7), which lead us to rule out this hypothesis because it would mean drifting toward both eastward and westward directions.

While the uncertainty derived from calibration and ΔR uncertainty in our independent age model captures the magnetic age model derived from correlation to the very-well dated GREENICE record, it is difficult to distinguish if the systematic offset to the median radiocarbon age model is actually related to reasonable centennial scale ΔR uncertainty/variability, ~10 cm scale NRM lock-in depth, or a combination of both. These factors and timescales are challenging to assess and this level of uncertainty may be the limit to which we can resolve time in Petermann Fjord sediments.

4.2. Paleointensity and Paleomagnetic Secular Variations in the Arctic and the Northern North Atlantic

Because of the uncertain reliability of the top interval, we will focus on the reconstitution of the PSV and VGP for the time period 0.7–6.3 ka, where the RPI and PSV signals of the stack are robust and reliable. In Figure 8, RPI signals for the U1305 site and Petermann stack are plotted with their magnetic age model (this study; Stoner et al., 2013), whereas other signals have an age model based on ^{14}C dates, which could explain some of the differences and offsets. Virtual Geomagnetic Poles (VGP) paleopositions (latitude, longitude) were calculated using the Mazaud Excel spreadsheet (Mazaud, 2005) from the Petermann PSV stack and are presented in Figure 10.

The directional PSV records discussed here are broadly similar and there is no clear relation between their variability and the position of these records relative to the surface projection of the TC. On the contrary, Arctic records are similar to northern North Atlantic records, whereas North American records are similar to European records, indicating that the TC is likely not the driver of these geomagnetic field feature variations. While declinations appear to be offsets between 3.7 and 6.1 ka (Figure 9c), angular (VGP or directions) differences between GREENICE and Petermann are between 0° and 25° for 0–6 ka and between 3° and 17° for the interval 3.7–6.1 ka, attesting to the similarities of these two records. Because of the steep inclinations (~85°), the importance of declination is debatable.

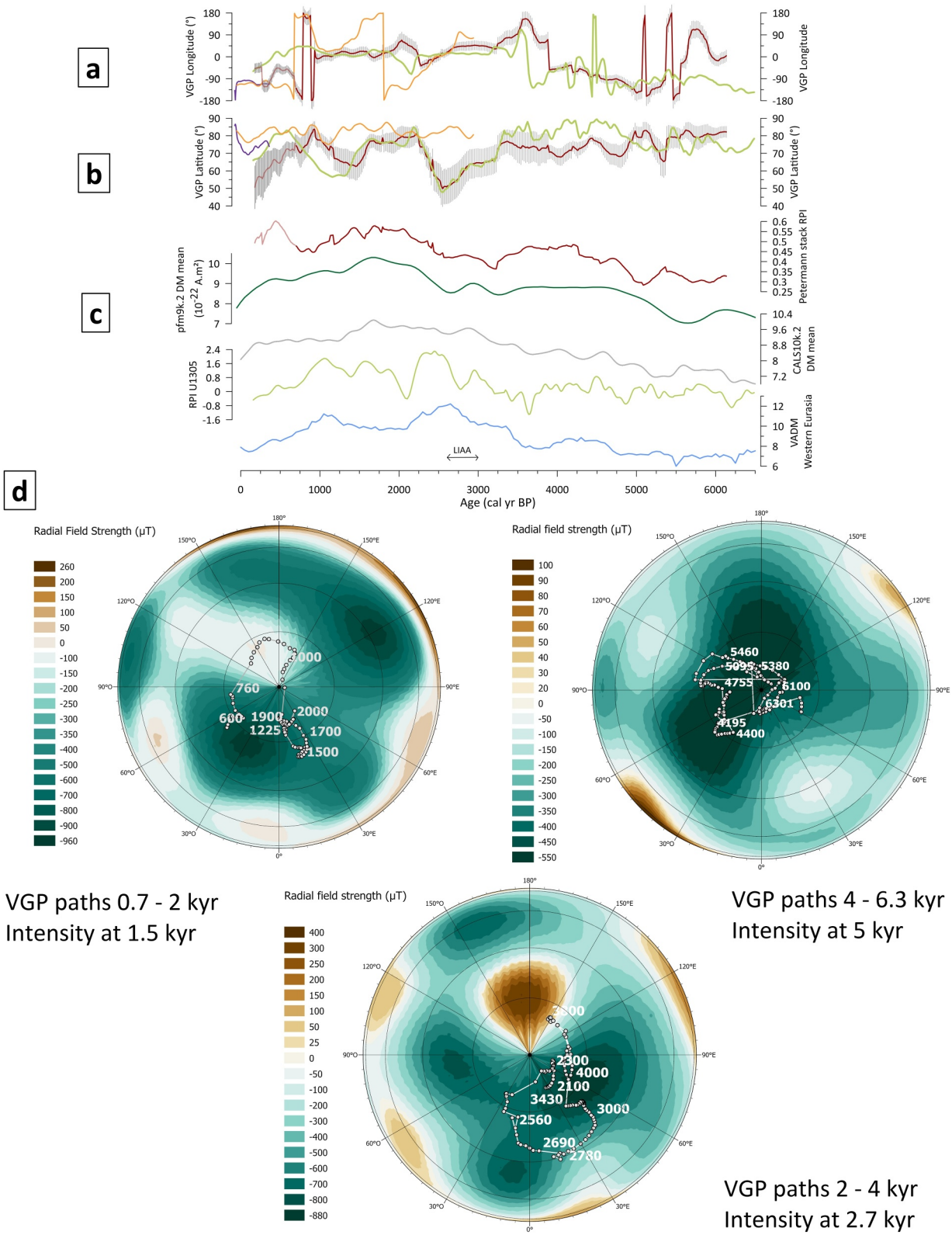

Figure 10.

Petermann RPI signal is similar to both the projections from the pfm9k.2 model for the site location (Figure 8) and the pfm9k.2 global dipole moment (Figure 10). This is remarkable given the limited amount of data from the Arctic used to build pfm9k.2. A change in the variation is observed in the record around 3.5 ka (0.5–3.5 ka: latitude varies between 45° and 85°; 3.5–6.3 ka: latitude varies between 65° and 85°). The model from Nilsson et al. (2022) described a mode shift from a 1,300 years periodicity to a 650 years periodicity, at the same time (3.6 ka). Further studies are needed to test if there is a link between what is described by the model and what we observe in our record. The phase difference between the Europe and Petermann intensity profiles (Figure 10) is consistent with the idea of east-west hemispherical field asymmetry resulting from the intensification of geomagnetic flux lobes (Gallet et al., 2009; Nilsson et al., 2022; Stoner et al., 2013). The pfm9k.2 model describes two particular periods of strong east-west field asymmetry, the time period around 1600–300 BCE (2.3–3.6 ka BP) is observed in our RPI record as a low intensity and low latitude VGPs. Petermann intensity and Western Europe VADM seem to be out of phase, while RPI at site U1305 and VADM from western Eurasia are in phase.

Comparing current variations (International Geomagnetic Reference Field; IGRF curves; Figure 10) to the Holocene records demonstrates that the recent NMP migration (Livermore et al., 2020; NOAA, 2021) does not seem abnormal with regard to the whole Holocene, as the VGP reconstruction from the Petermann stack and U1305 record display larger amplitude variations than the IGRF curve describing the recent variations. Nonetheless, it must be kept in mind that the IGRF depicts the variation of the actual NMP (dip pole), whereas the Holocene records reconstitute the Virtual Geomagnetic Pole position (north pole for a geomagnetic dipole). Differences between our record and the ARCH3k.1 model may be explained by the bias of the model toward mid-latitude in the Northern Hemisphere. VGP latitude variations prior to 3.5 ka have a similar amplitude to the recent variations displayed by the IGRF curve, whereas the U1305 and Petermann stack curves between 0.5 and 3.5 ka show greater amplitude variations. More past VGP variation data would allow a more definitive determination of ongoing NMP changes. Moreover, given that the declination is almost always relative, it is rather difficult to ascertain that the variations we are describing are the true paleo pole positions. VGP migrated within the surface projection of the TC for most of the last 6.3 ka, except for a large swing above Europe in the time interval 2.5–3.4 ka, and a smaller one around 1.3–1.6 ka. Another VGP path variation outside the TC is observed around 5.5 ka from the Petermann stack and from the NBS stack (Caricchi et al., 2020) but with a slight temporal offset (5.6 ka). It fits within the change of frequencies established by Nilsson et al. (2022). The uncertainties of the variation for that event are within the projection surface of the TC. A VGP migration above Greenland, within the TC surface projection (Figure 10), is observed at 4.2–4.4 ka in the Petermann stack but not in other paleorecords.

The 2.5–3 ka time interval of VGP migration at low latitude over Europe happening at a time of high intensity over Europe is coherent to what can be observed in other records such as GREENICE (Stoner et al., 2007, 2013), U1305 (Stoner et al., 2013) and the NBS stack from the Barents Sea (Caricchi et al., 2020). These studies, among others, suggested that variations in intensity, possibly driven by either the morphology or intensity of geomagnetic flux lobes, could play a role in VGP migration as a VGP attractor (Amit et al., 2011). However, high intensities are visible in Petermann Fjord and south Greenland (U1305) at 1.5–2 ka, but according to the projections, the Petermann VGP is located above Northern Europe, although the intensity is lower in that area. This could be because declination data are not accurate. The high intensity over Europe (2.5–3 ka) is coeval with the Levantine Iron Age Anomaly (LIAA), which was an intense positive geomagnetic anomaly in the Levant and Mediterranean regions (e.g., Shaar et al., 2016, 2017) characterized by a VADM of almost twice today's axial dipole moment (Shaar et al., 2017). If that played a role in the VGP migration at that time, it is an indication that a very high intensity is required to have that influence and the intensity over the Arctic was not high enough for that. Converting the Petermann RPI values into VADM would enable comparison of the intensities and ascertain the hypothesis because relative variations are more complex to compare than absolute values, and it is hard to determine if the anomalies are positive or negative. Moreover, Livermore et al. (2020) showed that the elongation and weakening of the North American flux lobe between 1970 and 1999 was responsible for the recent NMP

Figure 10. (a) Longitude variations of virtual geomagnetic poles based on the record's directional data. (b) Latitude variations of Virtual Geomagnetic Pole. Red = Petermann stack; purple = International Geomagnetic Reference Field; orange = ARCH3K.1; green = U1305. (c) Relative and absolute paleointensities curves in Petermann (red), Northern Atlantic (light green), over Europe (blue), and global dipole moment according to pfm9k.2 model (dark green, Nilsson et al., 2022) and CALS10k.2 model (gray, Constable et al., 2016). (d) Projection of VGP paths reconstructions based on Petermann stack directional data at time-intervals 0–2 ka; 2–4 ka; 4–6.3 ka overlaid on maps of radial field strength at Core Mantle Boundary from CALS10k.2 model respectively at 1.5, 2.7, 5 ka. The projections and maps were designed on ArcGIS.

migration acceleration toward Siberia, indicating that the intensity and size of the flux lobes may have an impact on the migration of the NMP. According to the pfm9k.2 geomagnetic model (Nilsson et al., 2022), a decrease in the global dipole moment can coincide with local intensity anomalies. Our data could be consistent with that hypothesis, with the example of the LIAA (Figure 10), which takes place when the global dipole moment and the Petermann RPI are decreasing (pfm9k.2 model; Figure 10). It could be the same phenomenon responsible for the recent migration of the NMP toward Siberia, with the growth of the geomagnetic flux lobe in that region (Livermore et al., 2020) and the recent decrease of the dipole moment (Gubbins et al., 2006). Our work supports the link between VGP incursions to lower latitude and strong field asymmetries, and additional studies are needed to test the hypothesis of a link between the intensity oscillation periodicity derived from pfm9k.2, NMP migration and field asymmetries. As all these hypotheses are based on a record at a very high latitude, it is not enough to draw firm conclusions. This shows that despite the Petermann record's potential, we need more data, including absolute intensity and accurate declination values (cores need to be oriented during coring).

5. Conclusions

This study illustrates that Petermann Fjord sediments record reproducible Holocene paleomagnetic secular variations that are similar throughout the Arctic. In particular, the shallow inclination at 2.5 ka is the most prominent feature of the last 7 kyr and is described in several records from the Arctic (Lund et al., 2016), the northern North Atlantic (Stoner et al., 2007, 2013) and geomagnetic model outputs (pfm9k.2; Nilsson et al., 2022). However, RPI variations in North Greenland are out-of-sync at millennial timescales with Southern Greenland, which looks more like European reconstructions (Stoner et al., 2013). There is good agreement between the Petermann RPI signal and local predictions and global dipole moment from the pfm9k.2 model, supporting the output of that model despite a lack of data from this region. These observations suggest that some directional PSV features that are well described and dated in several Arctic and northern North Atlantic records can be used as precise tie points to build Arctic chronologies where dating is challenging. This is consistent with findings from the very well-dated but lower resolution Lake Hajeren record from ~80°N in Svalbard (Ólafsdóttir et al., 2019). We recognize that the use of RPI at the centennial to millennial timescale, in this region, might require additional study to better understand its spatial pattern of variability.

Taken together, our results support the idea that Petermann Fjord is an excellent site to study PSV and RPI because it is located at a very high latitude with sediments characterized by high SAR capable of capturing the main millennial and secular variations of the Holocene. VGP reconstructions from this High Arctic geologic observatory display rapid NMP movements between the Eastern and Western Hemispheres, illustrating that recent variations of the historical periods are not abnormal and that such amplitudes of variations are consistent with Holocene variations and likely related to millennial scale dynamics of intensity anomalies of Northern Hemisphere Flux Lobes. Our work supports the hypothesis that magnetic field intensity variations linked to geomagnetic flux lobe variations could influence VGP migrations. Further full-vector paleomagnetic studies of high resolution and well-dated Arctic records will help improve our understanding of these dynamics, particularly conducting such studies on a larger scale to evaluate the extent of the influence of geomagnetic flux lobes.

Data Availability Statement

Paleomagnetic data (core AMD1902-10GC and updated Petermann stack) are archived in the PANGAEA database (Girard et al., 2024a, 2024b). Maps were made using ArcGIS with IBCAO bathymetric data. Figures using Golden Software Grapher 21. The age model was made using the R Bacon package.

Acknowledgments
We are grateful to the captain, officers, crew and scientists onboard both the CCGS Amundsen during the 2019 (Leg 2) ArcticNet expedition and the Swedish Icebreaker Oden during the Petermann 2015 Expedition for the recovery of the sediment cores used in this study. We also thank Quentin Beauvais (ISMER) for his help with the magnetic measurements; Dominique Lavallée (ISMER) for the grain size analysis; Nicole Sanderson (UQAM) for her help with the R package "rbacon"; Nicolas Van Nieuwenhove (UNB) for the foraminifera picking; and Arthur Bieber and Quentin Duboc (ISMER) for interesting discussions about the data. We also wish to thank the two anonymous reviewers and the editor Sonia Tikoo for their constructive comments that helped to improve the manuscripts. This research was funded by ArcticNet, the Canada Research Chair in Marine Geology from G. St-Onge, the Natural Sciences and Engineering Research Council of Canada (NSERC) through discovery grants to G. St-Onge and J.-C. Montero-Serrano, and the ISMER excellence scholarship and PBEEE-FRQNT scholarship n°334533 provided to J. Girard. J. Stoner and A. Jennings received support from the National Science Foundation Office of Polar Programs (awards 1417784 and 1418053).

References

Amit, H., Korte, M., Aubert, J., Constable, C., & Hulot, G. (2011). The time-dependence of intense archeomagnetic flux patches. *Journal of Geophysical Research*, *116*(B12), B12106. https://doi.org/10.1029/2011JB008538

Aurnou, J., Andreadis, S., Zhu, L., & Olson, P. (2003). Experiments on convection in Earth's core tangent cylinder. *Earth and Planetary Science Letters*, *212*(1–2), 119–134. https://doi.org/10.1016/S0012-821X(03)00237-1

Banerjee, S. K., King, J., & Marvin, J. (1981). A rapid method for magnetic granulometry with applications to environmental studies. *Geophysical Research Letters*, *8*(4), 333–336. https://doi.org/10.1029/GL008i004p00333

Barletta, F., St-Onge, G., Channell, J. E. T., & Rochon, A. (2010). Dating of Holocene western Canadian Arctic sediments by matching paleomagnetic secular variation to a geomagnetic field model. *Quaternary Science Reviews*, *29*(17–18), 2315–2324. https://doi.org/10.1016/j.quascirev.2010.05.035

Barletta, F., St-Onge, G., Stoner, J. S., Lajeunesse, P., & Locat, J. (2010). A high-resolution Holocene paleomagnetic secular variation and relative paleointensity stack from eastern Canada. *Earth and Planetary Science Letters*, *298*(1–2), 162–174. https://doi.org/10.1016/j.epsl.2010.07.038

Blaauw, M., & Christen, J. A. (2011). Flexible paleoclimate age-depth models using an autoregressive gamma process. *Bayesian Analysis*, *6*(3), 457–474. https://doi.org/10.1214/11-BA618

Bloemendal, J., Lamb, B., & King, J. (1988). Paleoenvironmental implications of rock magnetic properties of late quaternary sediment cores from the eastern equatorial Atlantic. *Paleoceanography*, *3*(1), 61–87. https://doi.org/10.1029/PA003i001p00061

Blott, S. J., & Pye, K. (2001). GRADISTAT: A grain size distribution and statistics package for the analysis of unconsolidated sediments. *Earth Surface Processes and Landforms*, *26*(11), 1237–1248. https://doi.org/10.1002/esp.261

Bloxham, J., & Gubbins, D. (1985). The secular variation of Earth's magnetic field. *Nature*, *317*(6040), 777–781. https://doi.org/10.1038/317777a0

Bloxham, J., Gubbins, D., & Jackson, A. (1989). Geomagnetic secular variation. *Philosophical Transactions of the Royal Society of London. Series A: Mathematical, Physical and Engineering Sciences*, *329*(1606), 415–502.

Bloxham, J., & Jackson, A. (1992). Time-dependent mapping of the magnetic field at the core-mantle boundary. *Journal of Geophysical Research*, *97*(B13), 19537–19563. https://doi.org/10.1029/92JB01591

Brown, M. C., Donadini, F., Korte, M., Nilsson, A., Korhonen, K., Lodge, A., et al. (2015). GEOMAGIA50.v3: 1. General structure and modifications to the archeological and volcanic database. *Earth, Planets and Space*, *67*(1), 83. https://doi.org/10.1186/s40623-015-0232-0

Caricchi, C., Sagnotti, L., Campuzano, S. A., Lucchi, R. G., Macrì, P., Rebesco, M., & Camerlenghi, A. (2020). A refined age calibrated paleosecular variation and relative paleointensity stack for the NW Barents Sea: Implication for geomagnetic field behavior during the Holocene. *Quaternary Science Reviews*, *229*, 106133. https://doi.org/10.1016/j.quascirev.2019.106133

Caron, M., St-Onge, G., Montero-Serrano, J.-C., Rochon, A., Georgiadis, E., Giraudeau, J., & Massé, G. (2019). Holocene chronostratigraphy of northeastern Baffin Bay based on radiocarbon and palaeomagnetic data. *Boreas*, *48*(1), 147–165. https://doi.org/10.1111/bor.12346

Channell, J. E. T., Stoner, J. S., Hodell, D. A., & Charles, C. D. (2000). Geomagnetic paleointensity for the last 100 kyr from the sub-Antarctic South Atlantic: A tool for inter-hemispheric correlation. *Earth and Planetary Science Letters*, *175*(1–2), 145–160. https://doi.org/10.1016/S0012-821X(99)00285-X

Chulliat, A., Hulot, G., & Newitt, L. R. (2010). Magnetic flux expulsion from the core as a possible cause of the unusually large acceleration of the north magnetic pole during the 1990s. *Journal of Geophysical Research*, *115*(B7), B07101. https://doi.org/10.1029/2009JB007143

Chulliat, A., Hulot, G., Newitt, L. R., & Orgeval, J.-J. (2010). What caused recent acceleration of the north magnetic pole drift? *Eos, Transactions American Geophysical Union*, *91*(51), 501–502. https://doi.org/10.1029/2010EO510001

Constable, C., Korte, M., & Panovska, S. (2016). Persistent high paleosecular variation activity in southern hemisphere for at least 10 000 years. *Earth and Planetary Science Letters*, *453*, 78–86. https://doi.org/10.1016/j.epsl.2016.08.015

Croudace, I. W. & Rothwell, R. G. (Eds.) (2015). *Micro-XRF studies of sediment cores: Applications of a non-destructive tool for the environmental sciences* (Vol. 17). Springer Netherlands. https://doi.org/10.1007/978-94-017-9849-5

Dankers, P. (1981). Relationship between median destructive field and remanent coercive forces for dispersed natural magnetite, titanomagnetite and hematite. *Geophysical Journal International*, *64*(2), 447–461. https://doi.org/10.1111/j.1365-246X.1981.tb02676.x

Dawes, P. R., Frisch, T., Garde, A. A., Iannelli, T. R., Ineson, J. R., Jensen, S. M., et al. (2000). Kane Basin 1999: Mapping, stratigraphic studies and economic assessment of Precambrian and Lower Palaeozoic provinces in north-western Greenland. *Geology of Greenland Survey Bulletin*, *186*, 11–28. https://doi.org/10.34194/ggub.v186.5211

Day, R., Fuller, M., & Schmidt, V. A. (1977). Hysteresis properties of titanomagnetites: Grain-size and compositional dependence. *Physics of the Earth and Planetary Interiors*, *13*(4), 260–267. https://doi.org/10.1016/0031-9201(77)90108-X

Debret, M., Sebag, D., Desmet, M., Balsam, W., Copard, Y., Mourier, B., et al. (2011). Spectrocolorimetric interpretation of sedimentary dynamics: The new "Q7/4 diagram". *Earth-Science Reviews*, *109*(1–2), 1–19. https://doi.org/10.1016/j.earscirev.2011.07.002

Detlef, H., Reilly, B., Jennings, A., Mørk Jensen, M., O'Regan, M., Glasius, M., et al. (2021). Holocene sea-ice dynamics in Petermann Fjord in relation to ice tongue stability and Nares Strait ice arch formation. *The Cryosphere*, *15*(9), 4357–4380. https://doi.org/10.5194/tc-15-4357-2021

Donadini, F., Korte, M., & Constable, C. G. (2009). Geomagnetic field for 0–3 ka: 1. New data sets for global modeling. *Geochemistry, Geophysics, Geosystems*, *10*(6), 2008GC002295. https://doi.org/10.1029/2008GC002295

Dumberry, M., & Finlay, C. C. (2007). Eastward and westward drift of the Earth's magnetic field for the last three millennia. *Earth and Planetary Science Letters*, *254*(1–2), 146–157. https://doi.org/10.1016/j.epsl.2006.11.026

Dunlop, D. J. (2002). Theory and application of the Day plot (Mrs/Ms versus Hcr/Hc) 1. Theoretical curves and tests using titanomagnetite data. *Journal of Geophysical Research*, *107*(B3), EPM4-1. https://doi.org/10.1029/2001JB000486

Dunlop, D. J., & Ozdemir, O. (2007). Magnetization in rocks and minerals. In *Geomagnetism, treatise on geophysics* (Vol. 5, pp. 277–336). Elsevier. G. Scubert. https://doi.org/10.1016/b978-044452748-6/00093-6

Fisher, R. (1953). Dispersion on a sphere. *Proceedings of the Royal Society A: Mathematical, Physical and Engineering Sciences*, *217*(1130), 295–305. https://doi.org/10.1098/rspa.1953.0064

Froelich, P. N., Klinkhammer, G. P., Bender, M. L., Luedtke, N. A., Heath, G. R., Cullen, D., et al. (1979). Early oxidation of organic matter in pelagic sediments of the eastern equatorial Atlantic: Suhoxic diagenesis. *Geochimica et Cosmochimica Acta*, *43*(7), 1075–1090. https://doi.org/10.1016/0016-7037(79)90095-4

Gallet, Y., Hulot, G., Chulliat, A., & Genevey, A. (2009). Geomagnetic field hemispheric asymmetry and archeomagnetic jerks. *Earth and Planetary Science Letters*, *284*(1–2), 179–186. https://doi.org/10.1016/j.epsl.2009.04.028

Gauss, C. F. (1833). Intensitas vis magneticae terrestris ad mensuram absolutam revocata.

Genevey, A., Gallet, Y., Constable, C. G., Korte, M., & Hulot, G. (2008). ArcheoInt: An upgraded compilation of geomagnetic field intensity data for the past ten millennia and its application to the recovery of the past dipole moment: Geomagnetic field intensity data compilation. *Geochemistry, Geophysics, Geosystems*, *9*(4), n/a. https://doi.org/10.1029/2007GC001881

Girard, J., Reilly, B. T., St-Onge, G., Lagroix, F., Montero-Serrano, J.-C., Stoner, J., & Jennings, A. E. (2024a). Paleomagnetic data (inclination, declination, relative paleointensity) in sediment core AMD1902-10GC from Petermann Fjord (Nares Strait, Northern Greenland) [Dataset]. Retrieved from https://doi.pangaea.de/10.1594/PANGAEA.971852

Girard, J., Reilly, B. T., St-Onge, G., Lagroix, F., Montero-Serrano, J.-C., Stoner, J., & Jennings, A. E. (2024b). Updated paleomagnetic Petermann stack (inclination, declination, relative paleointensity, Virtual Geomagnetic Pole) from Petermann Fjord (Nares Strait, Northern Greenland) [Dataset]. Retrieved from https://doi.pangaea.de/10.1594/PANGAEA.971851

Grobe, H. (1987). A simple method for the determination of Ice-Rafted Debris in sediment cores. *Polarforschung*, *57*, 123–126.

Gubbins, D. (2008). Geomagnetic reversals. *Nature*, *452*(7184), 165–167. https://doi.org/10.1038/452165a

Gubbins, D., Jones, A. L., & Finlay, C. C. (2006). Fall in Earth's magnetic field is erratic. *Science*, *312*(5775), 900–902. https://doi.org/10.1126/science.1124855

Hagen, C. J., Reilly, B. T., Stoner, J. S., & Creveling, J. R. (2020). Dynamic time warping of palaeomagnetic secular variation data. *Geophysical Journal International*, *221*(1), 706–721. https://doi.org/10.1093/gji/ggaa004

Haines, G. V., & Newitt, L. R. (1997). The Canadian geomagnetic reference field 1995. *Journal of Geomagnetism and Geoelectricity*, *49*(2), 317–336. https://doi.org/10.5636/jgg.49.317

Haltia-Hovi, E., Nowaczyk, N., & Saarinen, T. (2010). Holocene palaeomagnetic secular variation recorded in multiple lake sediment cores from eastern Finland. *Geophysical Journal International*, *180*(2), 609–622. https://doi.org/10.1111/j.1365-246X.2009.04456.x

Harrison, R. J., & Feinberg, J. M. (2008). FORCinel: An improved algorithm for calculating first-order reversal curve distributions using locally weighted regression smoothing: FORCinel algorithm. *Geochemistry, Geophysics, Geosystems*, *9*(5), n/a. https://doi.org/10.1029/2008GC001987

Heaton, T. J., Köhler, P., Butzin, M., Bard, E., Reimer, R. W., Austin, W. E. N., et al. (2020). Marine20—The marine radiocarbon age calibration curve (0–55,000 cal BP). *Radiocarbon*, *62*(4), 779–820. https://doi.org/10.1017/RDC.2020.68

Heuzé, C., Wåhlin, A., Johnson, H. L., & Münchow, A. (2017). Pathways of meltwater export from Petermann Glacier, Greenland. *Journal of Physical Oceanography*, *47*(2), 405–418. https://doi.org/10.1175/JPO-D-16-0161.1

Hogan, K. A., Jakobsson, M., Mayer, L., Reilly, B. T., Jennings, A. E., Stoner, J. S., et al. (2020). Glacial sedimentation, fluxes and erosion rates associated with ice retreat in Petermann Fjord and Nares Strait, north-west Greenland. *The Cryosphere*, *14*(1), 261–286. https://doi.org/10.5194/tc-14-261-2020

Hollerbach, R., & Jones, C. (1993). Influence of the Earth's inner core on geomagnetic fluctuations and reversals. *Nature*, *365*(6446), 541–543. https://doi.org/10.1038/365541a0

Hu, S., Appel, E., Hoffmann, V., Schmahl, W. W., & Wang, S. (1998). Gyromagnetic remanence acquired by greigite (Fe_3S_4) during static three-axis alternating field demagnetization: GRM acquired by greigite. *Geophysical Journal International*, *134*(3), 831–842. https://doi.org/10.1046/j.1365-246x.1998.00627.x

Hulot, G., Eymin, C., Langlais, B., Mandea, M., & Olsen, N. (2002). Small-scale structure of the geodynamo inferred from Oersted and Magsat satellite data. *Nature*, *416*(6881), 620–623. https://doi.org/10.1038/416620a

Jackson, A., Jonkers, A. R. T., & Walker, M. R. (2000). Four centuries of geomagnetic secular variation from historical records. *Philosophical Transactions of the Royal Society of London. Series A: Mathematical, Physical and Engineering Sciences*, *358*(1768), 957–990. https://doi.org/10.1098/rsta.2000.0569

Jakobsson, M., Hogan, K. A., Mayer, L. A., Mix, A., Jennings, A., Stoner, J., et al. (2018). The Holocene retreat dynamics and stability of Petermann Glacier in northwest Greenland. *Nature Communications*, *9*(1), 2104. https://doi.org/10.1038/s41467-018-04573-2

Jakobsson, M., Mayer, L. A., Bringensparr, C., Castro, C. F., Mohammad, R., Johnson, P., et al. (2020). The International Bathymetric Chart of the Arctic Ocean version 4.0. *Scientific Data*, *7*(1), 176. https://doi.org/10.1038/s41597-020-0520-9

Jennings, A. E., Reilly, B., Andrews, J., Hogan, K., Walczak, M., Jakobsson, M., et al. (2022). Modern and early Holocene ice shelf sediment facies from Petermann Fjord and northern Nares Strait, northwest Greenland. *Quaternary Science Reviews*, *283*, 107460. https://doi.org/10.1016/j.quascirev.2022.107460

Jennings, A. E., Seidenkrantz, M.-S., & Knudsen, K. L. (2020). Glomulina oculus, new calcareous foraminiferal species from the High Arctic: A potential indicator of a nearby marine-terminating glacier. *Journal of Foraminiferal Research*, *50*(2), 219–234. https://doi.org/10.2113/gsjfr.52.2.219

Johnson, H. L., Münchow, A., Falkner, K. K., & Melling, H. (2011). Ocean circulation and properties in Petermann Fjord, Greenland. *Journal of Geophysical Research*, *116*(C1), C01003. https://doi.org/10.1029/2010JC006519

Khokhlov, A., & Hulot, G. (2016). Principal component analysis of palaeomagnetic directions: Converting a Maximum Angular Deviation (MAD) into an α95 angle. *Geophysical Journal International*, *204*(1), 274–291. https://doi.org/10.1093/gji/ggv451

King, J. W., Banerjee, S. K., & Marvin, J. (1983). A new rock-magnetic approach to selecting sediments for geomagnetic paleointensity studies: Application to paleointensity for the last 4000 years. *Journal of Geophysical Research*, *88*(B7), 5911–5921. https://doi.org/10.1029/JB088iB07p05911

King, J. W., Banerjee, S. K., Marvin, J., & Özdemir, Ö. (1982). A comparison of different magnetic methods for determining the relative grain size of magnetite in natural materials: Some results from lake sediments. *Earth and Planetary Science Letters*, *59*(2), 404–419. https://doi.org/10.1016/0012-821X(82)90142-X

Kirschvink, J. L. (1980). The least-squares line and plane and the analysis of palaeomagnetic data. *Geophysical Journal International*, *62*(3), 699–718. https://doi.org/10.1111/j.1365-246X.1980.tb02601.x

Korte, M., & Constable, C. G. (2018). Archeomagnetic intensity spikes: Global or regional geomagnetic field features? *Frontiers in Earth Science*, *6*, 17. https://doi.org/10.3389/feart.2018.00017

Kotov, S., & Pälike, H. (2018). QAnalySeries – A cross-platform time series tuning and analysis tool. *ESS Open Archive*. https://doi.org/10.1002/essoar.10500226.1

Lawrence, K. P., Tauxe, L., Staudigel, H., Constable, C. G., Koppers, A., McIntosh, W., & Johnson, C. L. (2009). Paleomagnetic field properties at high southern latitude. *Geochemistry, Geophysics, Geosystems*, *10*(1), Q01005. https://doi.org/10.1029/2008GC002072

Lévesque, Y., St-Onge, G., Lajeunesse, P., Desiage, P., & Brouard, E. (2020). Defining the maximum extent of the Laurentide Ice Sheet in Home Bay (eastern Arctic Canada) during the Last Glacial episode. *Boreas*, *49*(1), 52–70. https://doi.org/10.1111/bor.12415

Livermore, P. W., Finlay, C. C., & Bayliff, M. (2020). Recent north magnetic pole acceleration towards Siberia caused by flux lobe elongation. *Nature Geoscience*, *13*(5), 387–391. https://doi.org/10.1038/s41561-020-0570-9

Lund, S., Keigwin, L., & Darby, D. (2016). Character of Holocene paleomagnetic secular variation in the tangent cylinder: Evidence from the Chukchi Sea. *Physics of the Earth and Planetary Interiors*, *256*, 49–58. https://doi.org/10.1016/j.pepi.2016.03.005

Maxbauer, D. P., Feinberg, J. M., & Fox, D. L. (2016). MAX UnMix: A web application for unmixing magnetic coercivity distributions. *Computers & Geosciences*, *95*, 140–145. https://doi.org/10.1016/j.cageo.2016.07.009

Mazaud, A. (2005). User-friendly software for vector analysis of the magnetization of long sediment cores: Software for vector analysis. *Geochemistry, Geophysics, Geosystems*, *6*(12), n/a. https://doi.org/10.1029/2005GC001036

Montero-Serrano, J.-C., & Brossard, J. (2019). Cruise report: Collecting sedimentary sequences and plankton samples in the continental margins from the eastern Canadian Arctic Archipelago. [Cruise Report] (p. 22).

Münchow, A., Falkner, K. K., Melling, H., Rabe, B., & Johnson, H. L. (2011). Ocean warming of Nares Strait bottom waters off northwest Greenland. 2003-2009. *Oceanography*, *24*(3), 114–123. https://doi.org/10.5670/oceanog.2011.62

Münchow, A., Padman, L., Washam, P., & Nicholls, K. (2016). The Ice Shelf of Petermann Gletscher, North Greenland, and its connection to the Arctic and Atlantic Oceans. *Oceanography*, *29*(4), 84–95. https://doi.org/10.5670/oceanog.2016.101

National Centers for Environmental Information. (2022). State of the geomagnetic field 2022. https://doi.org/10.25923/8R5D-FJ70

National Centers for Environmental Information (U.S.). (2023). State of the geomagnetic field 2023. https://doi.org/10.25923/CWW1-SC35

Newitt, L. R., Mandea, M., McKee, L. A., & Orgeval, J.-J. (2002). Recent acceleration of the north magnetic pole linked to magnetic jerks. *Eos, Transactions American Geophysical Union*, *83*(35), 381–389. https://doi.org/10.1029/2002EO000276

Nilsson, A., Suttie, N., Korte, M., Holme, R., & Hill, M. (2020). Persistent westward drift of the geomagnetic field at the core–mantle boundary linked to recurrent high-latitude weak/reverse flux patches. *Geophysical Journal International*, *222*(2), 1423–1432. https://doi.org/10.1093/gji/ggaa249

Nilsson, A., Suttie, N., Stoner, J. S., & Muscheler, R. (2022). Recurrent ancient geomagnetic field anomalies shed light on future evolution of the South Atlantic Anomaly. *Proceedings of the National Academy of Sciences*, *119*(24), e2200749119. https://doi.org/10.1073/pnas.2200749119

NOAA. (2021). State of the geomagnetic field. WMM Annual Report, 13.

Ólafsdóttir, S., Reilly, B. T., Bakke, J., Stoner, J. S., Gjerde, M., & Van Der Bilt, W. G. M. (2019). Holocene paleomagnetic secular variation (PSV) near 80° N, Northwest Spitsbergen, Svalbard: Implications for evaluating High Arctic sediment chronologies. *Quaternary Science Reviews*, *210*, 90–102. https://doi.org/10.1016/j.quascirev.2019.03.003

Olsen, N., & Mandea, M. (2007). Will the magnetic North Pole move to Siberia? *Eos, Transactions American Geophysical Union*, *88*(29), 293. https://doi.org/10.1029/2007EO290001

Olson, P., & Aurnou, J. (1999). A polar vortex in the Earth's core. *Nature*, *402*(6758), 170–173. https://doi.org/10.1038/46017

Pearce, C., Özdemir, K. S., Forchhammer Mathiasen, R., Detlef, H., & Olsen, J. (2023). The marine reservoir age of Greenland coastal waters. *Geochronology*, *5*(2), 451–465. https://doi.org/10.5194/gchron-5-451-2023

Philippe, É. G. H., Valet, J., St-Onge, G., & Thevarasan, A. (2018). Are paleomagnetic records from U-channels appropriate for studies of reversals and excursions? *Geochemistry, Geophysics, Geosystems*, *19*(11), 4130–4142. https://doi.org/10.1029/2018GC007803

Pieńkowski, A. J., Coulthard, R. D., & Furze, M. F. A. (2022). Revised marine reservoir offset (ΔR) values for molluscs and marine mammals from Arctic North America. *Boreas*, *52*(2), 145–167. https://doi.org/10.1111/bor.12606

Reilly, B. T., Stoner, J. S., Hatfield, R. G., Abbott, M. B., Marchetti, D. W., Larsen, D. J., et al. (2018). Regionally consistent Western North America paleomagnetic directions from 15 to 35 ka: Assessing chronology and uncertainty with paleosecular variation (PSV) stratigraphy. *Quaternary Science Reviews*, *201*, 186–205. https://doi.org/10.1016/j.quascirev.2018.10.016

Reilly, B. T., Stoner, J. S., Mix, A. C., Walczak, M. H., Jennings, A., Jakobsson, M., et al. (2019). Holocene break-up and reestablishment of the Petermann Ice Tongue, Northwest Greenland. *Quaternary Science Reviews*, *218*, 322–342. https://doi.org/10.1016/j.quascirev.2019.06.023

Reilly, B. T., Stoner, J. S., Ólafsdóttir, S., Jennings, A., Hatfield, R., Kristjánsdóttir, G. B., & Geirsdóttir, Á. (2023). The amplitude and timescales of 0–15 ka paleomagnetic secular variation in the Northern North Atlantic. *Journal of Geophysical Research: Solid Earth*, *128*(6), e2023JB026891. https://doi.org/10.1029/2023JB026891

Roberts, A. P., Almeida, T., Church, N. S., Harrison, R. J., Heslop, D., Li, Y., et al. (2017). Resolving the origin of pseudo-single domain magnetic behavior. *Journal of Geophysical Research: Solid Earth*, *122*(12), 9534–9558. https://doi.org/10.1002/2017JB014860

Roberts, A. P., Heslop, D., Zhao, X., Oda, H., Egli, R., Harrison, R. J., et al. (2022). Unlocking information about fine magnetic particle assemblages from first-order reversal curve diagrams: Recent advances. *Earth-Science Reviews*, *227*, 103950. https://doi.org/10.1016/j.earscirev.2022.103950

Roberts, A. P., Hu, P., Harrison, R. J., Heslop, D., Muxworthy, A. R., Oda, H., et al. (2019). Domain state diagnosis in rock magnetism: Evaluation of potential alternatives to the day diagram. *Journal of Geophysical Research: Solid Earth*, *124*(6), 5286–5314. https://doi.org/10.1029/2018JB017049

Ross, J. C. (1834). III. On the position of the north magnetic pole. *The Royal Society*, *124*, 47–52. https://doi.org/10.1098/rstl.1834.0005

Shaar, R., Tauxe, L., Goguitchaichvili, A., Devidze, M., & Licheli, V. (2017). Further evidence of the Levantine Iron Age geomagnetic anomaly from Georgian pottery. *Geophysical Research Letters*, *44*(5), 2229–2236. https://doi.org/10.1002/2016GL071494

Shaar, R., Tauxe, L., Ron, H., Ebert, Y., Zuckerman, S., Finkelstein, I., & Agnon, A. (2016). Large geomagnetic field anomalies revealed in Bronze to Iron Age archeomagnetic data from Tel Megiddo and Tel Hazor, Israel. *Earth and Planetary Science Letters*, *442*, 173–185. https://doi.org/10.1016/j.epsl.2016.02.038

Simon, Q., Bourlès, D. L., Thouveny, N., Horng, C.-S., Valet, J.-P., Bassinot, F., & Choy, S. (2018). Cosmogenic signature of geomagnetic reversals and excursions from the Réunion event to the Matuyama–Brunhes transition (0.7–2.14 Ma interval). *Earth and Planetary Science Letters*, *482*, 510–524. https://doi.org/10.1016/j.epsl.2017.11.021

Simon, Q., St-Onge, G., & Hillaire-Marcel, C. (2012). Late Quaternary chronostratigraphic framework of deep Baffin Bay glaciomarine sediments from high-resolution paleomagnetic data. *Geochemistry, Geophysics, Geosystems*, *13*(11), 2012GC004272. https://doi.org/10.1029/2012GC004272

Simon, Q., Thouveny, N., Bourlès, D. L., Nuttin, L., Hillaire-Marcel, C., & St-Onge, G. (2016). Authigenic $^{10}Be/^{9}Be$ ratios and ^{10}Be-fluxes ($^{230}Th_{xs}$-normalized) in central Baffin Bay sediments during the last glacial cycle: Paleoenvironmental implications. *Quaternary Science Reviews*, *140*, 142–162. https://doi.org/10.1016/j.quascirev.2016.03.027

Stoner, J. S., Channell, J. E. T., & Hillaire-Marcel, C. (1995). Late Pleistocene relative geomagnetic paleointensity from the deep Labrador Sea: Regional and global correlations. *Earth and Planetary Science Letters*, *134*(3–4), 237–252. https://doi.org/10.1016/0012-821X(95)00134-X

Stoner, J. S., Channell, J. E. T., Hillaire-Marcel, C., & Kissel, C. (2000). Geomagnetic paleointensity and environmental record from Labrador Sea core MD95-2024: Global marine sediment and ice core chronostratigraphy for the last 110 kyr. *Earth and Planetary Science Letters*, *183*(1–2), 161–177. https://doi.org/10.1016/S0012-821X(00)00272-7

Stoner, J. S., Channell, J. E. T., Mazaud, A., Strano, S. E., & Xuan, C. (2013). The influence of high-latitude flux lobes on the Holocene paleomagnetic record of IODP Site U1305 and the northern North Atlantic: Paleomagnetic Record of the N. Atlantic. *Geochemistry, Geophysics, Geosystems*, *14*(10), 4623–4646. https://doi.org/10.1002/ggge.20272

Stoner, J. S., Jennings, A., Kristjánsdóttir, G. B., Dunhill, G., Andrews, J. T., & Hardardóttir, J. (2007). A paleomagnetic approach toward refining Holocene radiocarbon-based chronologies: Paleoceanographic records from the north Iceland (MD99-2269) and east Greenland (MD99-2322) margins: Holocene PSV and radiocarbon chronology. *Paleoceanography*, *22*(1), n/a. https://doi.org/10.1029/2006PA001285

Stoner, J. S., & St-Onge, G. (2007). Chapter Three Magnetic stratigraphy in paleoceanography: Reversals, excursions, paleointensity, and secular variation. In C. Hillaire–Marcel & A. De Vernal (Eds.), *Developments in marine geology* (Vol. 1, pp. 99–138). Elsevier. https://doi.org/10.1016/S1572-5480(07)01008-1

St-Onge, G., Mulder, T., Francus, P., & Long, B. (2007). Chapter Two Continuous physical properties of cored marine sediments. In *Developments in marine geology* (Vol. 1, pp. 63–98). Elsevier. https://doi.org/10.1016/S1572-5480(07)01007-X

St-Onge, G., & Stoner, J. (2011). Paleomagnetism near the north magnetic pole: A unique vantage point for understanding the dynamics of the geomagnetic field and its secular variations. *Oceanography*, *24*(3), 42–50. https://doi.org/10.5670/oceanog.2011.53

St-Onge, G., Stoner, J. S., & Hillaire-Marcel, C. (2003). Holocene paleomagnetic records from the St. Lawrence Estuary, eastern Canada: Centennial- to millennial-scale geomagnetic modulation of cosmogenic isotopes. *Earth and Planetary Science Letters*, *209*(1–2), 113–130. https://doi.org/10.1016/S0012-821X(03)00079-7

Suganuma, Y., Yokoyama, Y., Yamazaki, T., Kawamura, K., Horng, C.-S., & Matsuzaki, H. (2010). ^{10}Be evidence for delayed acquisition of remanent magnetization in marine sediments: Implication for a new age for the Matuyama–Brunhes boundary. *Earth and Planetary Science Letters*, *296*(3–4), 443–450. https://doi.org/10.1016/j.epsl.2010.05.031

Tauxe, L. (1993). Sedimentary records of relative paleointensity of the geomagnetic field: Theory and practice. *Reviews of Geophysics*, *31*(3), 319–354. https://doi.org/10.1029/93RG01771

Tauxe, L. (2010). *Essentials of paleomagnetism*. University of Columbia Press. https://doi.org/10.1525/9780520946378

Tauxe, L., Mullender, T. A. T., & Pick, T. (1996). Potbellies, wasp-waists, and superparamagnetism in magnetic hysteresis. *Journal of Geophysical Research*, *101*(B1), 571–583. https://doi.org/10.1029/95JB03041

Tauxe, L., Pick, T., & Kok, Y. S. (1995). Relative paleointenisty in sediments: A pseudo-Thellier approach. *Geophysical Research Letters*, *22*(21), 2885–2888. https://doi.org/10.1029/95GL03166

Tauxe, L., & Wu, G. (1990). Normalized remanence in sediments of the western equatorial Pacific: Relative paleointensity of the geomagnetic field? *Journal of Geophysical Research*, *95*(B8), 12337–12350. https://doi.org/10.1029/JB095iB08p12337

Thouveny, N. (1988). High-resolution palaeomagnetic study of Late Pleistocene sediments from Baffin Bay: First results. *Canadian Journal of Earth Sciences*, *25*(6), 833–843. https://doi.org/10.1139/e88-082

Valet, J.-P., & Meynadier, L. (1998). A comparison of different techniques for relative paleointensity. *Geophysical Research Letters*, *25*(1), 89–92. https://doi.org/10.1029/97GL03489

Velle, J. H., Walczak, M. H., Reilly, B., St-Onge, G., Stoner, J. S., Fallon, S., et al. (2021). High resolution inclination records from the Gulf of Alaska, IODP Expedition 341 Sites U1418 and U1419. *Geophysical Journal International*, *229*(1), 345–358. https://doi.org/10.1093/gji/ggab479

Washam, P., Nicholls, K. W., Münchow, A., & Padman, L. (2019). Summer surface melt thins Petermann Gletscher Ice Shelf by enhancing channelized basal melt. *Journal of Glaciology*, *65*(252), 662–674. https://doi.org/10.1017/jog.2019.43

Weeks, R., Laj, C., Endignoux, L., Fuller, M., Roberts, A., Manganne, R., et al. (1993). Improvements in long-core measurement techniques: Applications in palaeomagnetism and palaeoceanography. *Geophysical Journal International*, *114*(3), 651–662. https://doi.org/10.1111/j.1365-246X.1993.tb06994.x

Xuan, C., & Channell, J. E. T. (2009). UPmag: MATLAB software for viewing and processing u channel or other pass-through paleomagnetic data. *Geochemistry, Geophysics, Geosystems*, *10*(10), Q10Y07. https://doi.org/10.1029/2009GC002584

Yukutake, T. (1967). Dominion Observatory, Ottawa, Canada (p. 14). (Received February 18, 1967).

Zijderveld, J. (1967). AC demagnetisation of rocks: Analysis of results. In *Methods in paleomagnetism*.